Physics – Uspekhi **62** (8) 795 – 822 (2019)

REVIEWS OF TOPICAL PROBLEMS

PACS numbers: 75.30.Kz, 75.50.Bb, 75.50.Gg, **75.76.+j**, 75.78.Jp, 76.70.Hb, 78.30.Fs, 78.55.Et, **85.75.–d**

Spintronics of semiconductor, metallic, dielectric, and hybrid structures

(100th anniversary of the Ioffe Institute)

P G Baranov, A M Kalashnikova, V I Kozub, V L Korenev, Yu G Kusrayev, R V Pisarev, V F Sapega, I A Akimov, M Bayer, A V Scherbakov, D R Yakovlev

DOI: https://doi.org/10.3367/UFNe.2018.11.038486

Contents

Abstract. Demands for miniaturization, increasing the operation speed and energy efficiency of electronic devices led to the emergence and rapid development of spin electronics, or spintronics. Several areas of experimental and theoretical research are considered, in which the Ioffe Institute is actively involved. We discuss current progress in developing semiconductor and hybrid structures that exhibit specified magnetic properties, the development of methods for manipulating individual spins, a theoretical description of switching of metallic heterostructures magnetization by an electric field, and ultrafast control of magnetization via manipulating the magnetic anisotropy by femtosecond laser pulses.

P G Baranov [1], **A M Kalashnikova** [1,*], **V I Kozub** [1], **V L Korenev** [1], **Yu G Kusrayev** [1], **R V Pisarev** [1], **V F Sapega** [1], **I A Akimov** [1,2], **M Bayer** [1,2], **A V Scherbakov** [1,2], **D R Yakovlev** [1,2]
[1] Ioffe Institute, ul. Politekhnicheskaya 26, 194021 St. Petersburg, Russian Federation
[2] Experimental Physics II, TU Dortmund, Otto-Hahn str. 4, D-44227 Dortmund, Germany
E-mail: [*] kalashnikova@mail.ioffe.ru

Received 7 September 2018, revised 19 September 2018
Uspekhi Fizicheskikh Nauk **189** (8) 849 – 880 (2019)
DOI: https://doi.org/10.3367/UFNr.2018.11.038486
Translated by Yu V Morozov; edited by V L Derbov

Keywords: spin polarization, spin transport, ferromagnetic proximity effect, optically-detected magnetic resonance, laser-induced ultrafast magnetization dynamics, single spins, spin reorientation transitions, magnetic anisotropy, diluted magnetic semiconductors, ferromagnets, ferrimagnets

1. Introduction

Spin electronics or spintronics [1] is intended to solve the problem of information processing and transmission using the spin of electrons and other quasiparticles rather than charge transfer employed in traditional electronics. A few lines of research are currently distinguished in spintronics solving the problem of creation and readout of required spin states in nanostructures and their control by either an external magnetic field or an alternative stimulus. Modern spintronics deals with a wide variety of magnetic states, from single spins to antiferromagnetic spin ensembles coupled by exchange interactions. Moreover, the media for spintronics now include not only 'traditional' semiconductors and metals but also dielectrics that have long remained beyond consideration.

Studies on *semiconductor spintronics* [2, 3] are aimed to find new methods for generating and utilizing spin-polarized carriers, including spin transport, optical orientation, development of spin polarizers, amplifiers, spin valves, and other

multifunctional devices. Semiconductor-based spintronic devices are easy to integrate into traditional semiconductor electronics. One of the promising trends in semiconductor spintronics is the integration of semiconductor logic and magnetic memory using new hybrid semiconductor/ferromagnet devices capable of performing both logic and memory functions and manufactured in an integral technological process. An important aspect of semiconductor spintronics is the possibility of using various materials with predetermined properties, such as low-dimensional structures or diluted magnetic semiconductors. For example, two-dimensional structures (quantum wells) permit varying spin-orbit interaction, while quantum dots are characterized by long spin relaxation times.

A new era in semiconductor spintronics came along with the achievement of the ultimate level of miniaturization thanks to the creation of devices based on a single atom, a molecule, a defect, and, finally, a spin. This fantastic scenario is beginning to be implemented owing to the discovery of unique optical and magnetic properties of certain defects in diamond and silicon carbide, as well as to the development of methods allowing the registration of single spins at room temperature. Manipulating the spin states of a single atomic-size center at room temperature became possible due to optically detectable magnetic resonance of an isolated spin realized using a unique cycle of optical alignment of spin level populations. Single spin color centers in diamond and silicon carbide are currently regarded as a basis for creating a new generation of atomic-size quantum devices.

The rapid development of *metal-based spintronics* is largely associated with the discovery of the giant magnetoresistance effect in thin metal films, i.e., sensitivity of resistance of individual charge carriers to the mutual orientation of their spins and sample magnetization [4, 5]. The Nobel Prize in Physics 2007 was awarded jointly to Albert Fert and Peter Grünberg for this discovery. The further development of magnetoresistance research resulted in the discovery of various types of this phenomenon and eventually to the creation of new sensors [6] for the reading heads of magnetic hard disks. Spintronic phenomena in ferromagnetic metals not only found application in real information processing systems but also provided a basis for the functioning of advanced elements of spintronic devices, such as random-access magnetic storage cells [7], race-track memory [8], spin-transfer nanooscillators [9], etc.

The development of technologies for the production of heterostructures, the enhanced potential of experimental techniques, and theoretical methods for the description and prediction of their properties not only promoted further progress in the aforementioned classical fields of spintronics but also resulted in the appearance of two new research areas: *magnon spintronics* [10, 11] and *antiferromagnetic spintronics* [12, 13]. The novelty of magnon spintronics is that the role of an angular momentum carrier is played by quasiparticles called magnons, i.e., spin wave quanta. This, e.g., allows angular momentum transfer in dielectrics without the ohmic losses inevitable in metals and semiconductors. The development of antiferromagnetic spintronics may lead to further progress in the high-speed performance of spintronic devices due to sub- and terahertz frequencies of magnetic resonances in antiferromagnets.

Spintronics faces two challenging problems that are attracting the attention of many researchers. One is obtaining materials and structures with the desired and well-controlled states of single spins and their ensembles. The other important fundamental and applied problem is manipulation of individual spins and ensembles of uncoupled and coupled spins combining a high degree of spatial localization and a high rate of spin state variation. Of great interest are spin control methods based on the use of electric fields [14, 15], currents, strains, thermal gradients [16], and laser pulses [17] without application of an external magnetic field. The present review considers several conspicuous phenomena of significance for the improvement of existing and the creation of new elements of spintronic devices. We do not confine ourselves to a discussion of investigations conducted at the Ioffe Institute alone and lay emphasis on more general aspects of spintronic research to which scientists at the Ioffe Institute have made an important contribution.

Sections 2–4, devoted to semiconductor spintronics, consider two ultimate problems, one concerning the creation of ordered spin ensembles, the other single spin manipulation. Section 2 considers ferromagnetic ordering in diluted magnetic semiconductors (DMSs), such as (Ga,Mn)As. Another approach to the integration of magnetism into semiconductor electronics is presented in Section 3, where equilibrium and dynamic proximity effects in ferromagnetic metal/nonmagnetic semiconductor heterostructures (FM/SC) are discussed. In principle, such systems make it possible to control spin polarization in a semiconductor through the influence of the ferromagnet and, conversely, to regulate ferromagnet magnetization via the influence of the semiconductor. Also discussed in Section 3 are the interaction between elements of such hybrid systems and the distances at which it occurs. Section 4 is devoted to one of the recent trends in semiconductor spintronics, the single spin manipulations in diamond and silicon carbide by the optically-detected magnetic resonance technique.

Methods of control of the state of magnetically-ordered structures are considered in Sections 5 and 6. Control over magnetization of individual elements of ferromagnetic metal structures by electric field pulses is discussed in Section 5 with special emphasis on effects associated with spin injection from one ferromagnetic element into another and the influence of electric potential on indirect exchange between individual ferromagnet elements. Moreover, conditions are determined under which this effect can be realized in the absence of an electric current through the system; it permits significantly reducing the losses. Next, the effect of ultrafast current-induced switching of magnetization is considered in composite heterostructures based on the generation of a strongly nonequilibrium state upon a rise in electron temperature. Besides high-speed performance, this effect provides essential reduction of losses, because the integral absorbed energy appears to be not large.

Section 6 is focused on the solution to the problem of speed and efficiency of nanostructure magnetic state control by femtosecond laser pulses. We consider one large class of femtomagnetic events, namely, the laser-induced control of magnetic anisotropy with reference to ways to implement it in materials with different electronic and magnetic structures, from dielectrics to metals and from ferromagnets to antiferromagnets. Also discussed are magnetization switching based on ultrafast control of magnetic anisotropy, generation of spin transport and high-frequency magnetic fields localized at nanometer scales.

2. Hot photoluminescence and inelastic spin-flip light scattering in diluted magnetic semiconductors

2.1 Diluted magnetic semiconductors

Three approaches to implementation of semiconductor spintronic devices are currently considered. They are based on the use of hybrid ferromagnetic metal/semiconductor structures (see Section 3), diluted magnetic/ferromagnetic semiconductors with properties of semiconductors and ferromagnets, and magnetic semiconductors integrable into silicon electronics [18]. This section is devoted to the unique properties of diluted magnetic/ferromagnetic semiconductors (DMSs/DFSs). These properties are intrinsic in group II–VI, III–V, IV–VI, and IV Mn-doped semiconductors exhibiting ferromagnetic ordering in the Mn ion ensemble.

In the 1980s diluted magnetic semiconductors (Cd,Mn)Te and (Zn,Mn)Se were obtained that demonstrated strong magnetooptical effects [19]. Ferromagnetism induced by charge carriers was demonstrated for the first time in the group IV–VI semiconductor (Pb,Sn,Mn)Te [20]. A strong magnetooptical effect was also observed in GaAs:Mn [21], where huge enhancement of photoluminescence polarization occurred due to exchange interaction between holes bound to the Mn ion acceptor and electrons of its $3d^5$-shell (p–d-exchange). The p–d-exchange proved to be antiferromagnetic in character, as confirmed in many investigations [22–26]. The pronounced exchange interaction between holes and d-electrons of the Mn ion suggested the formation of ferromagnetic order in strongly-doped samples, because Mn is an acceptor impurity delivering into GaAs both localized magnetic moments and holes capable of transferring spin polarization between localized magnetic moments. However, the segregation capability of Mn at high concentrations and growth temperatures typical of GaAs did not for a long time allow the realization of the DFS regime in this system.

The breakthrough occurred in the 1990s when (In,Mn)As and (Ga,Mn)As were successfully grown by molecular-beam epitaxy at low temperatures [27–31] and hole-induced ferromagnetism was demonstrated. This discovery gave rise to extensive studies of such materials, which proved to be highly compatible with semiconductor electronics based on group III–V semiconductors. At present, they play the role of prototypes of a number of semiconductor spintronic devices. A disadvantage of DFS (Ga,Mn)As is the rather low Curie temperature, $T_C = 200$ K [32]. Nevertheless, the work of several spintronic elements based on this compound has been recently demonstrated [33–36] along with a few spin-dependent phenomena suitable, in principle, for applications [37–41].

Despite extensive experimental and theoretical studies on DFSs (Ga,Mn)As initiated in the late 1990s, the nature of ferromagnetism remains poorly understood, which prevents monitoring its properties and their efficient control. The majority of modern models suggests that holes play the key role in the formation of ferromagnetic order in (Ga,Mn)As. However, the state of these holes is still unclear. The most popular theoretical approach proposed in [42] explains ferromagnetism in (Ga,Mn)As in terms of the mean-field Zener model, suggesting that exchange p–d interaction of mobile (degenerate) holes of the valence band with localized Mn ions leads to the formation of ferromagnetic order. A number of (Ga,Mn)As properties were explained in the framework of this model [43–45]. On the other hand, optical [46–49] and transport [50, 51] experiments showed that the Fermi level of holes responsible for ferromagnetism lies in the impurity band. Therefore, in order to explain the experiments on tunnel transport through the (Ga,Mn)As layer, the authors of Ref. [52] discussed, as one of the alternatives, the Zener double-exchange model in which the ferromagnetic order arises as a result of hopping of spin-polarized holes [53].

Sections 2.2, 2.3 present results of DFS (Ga,Mn)As optical studies with the use of polarization magneto- and piezo-spectroscopy and inelastic spin-flip light scattering. These studies provided important information on the exchange field affecting holes and its uniaxial deformation dependence, coefficient of hole spin diffusion, and renormalization of the Mn ion g-factor. The low-temperature growth is known to result in a large number of radiationless recombination centers (with the lifetime $\tau \sim 10^{-13}-10^{-12}$ s) [54, 55] that completely quench usual edge luminescence. For this reason, the informative luminescent method has not thus far been used to study this material. On the other hand, effective nonradiative recombination fails to quench the luminescence of hot electrons (hot photoluminescence (HPL)) [48, 56], which allowed using this technique to clarify the magnetic properties of (Ga,Mn)As.

2.2 Polarized hot photoluminescence in (Ga,Mn)As

The solid curves in Figs 1a and 1b represent HPL spectra measured using paramagnetic (PM) and ferromagnetic (FM) samples of (Ga,Mn)As, respectively. Mn content in PM and FM samples was $x = 0.008$ and $x = 0.043$, respectively. Epitaxial $Ga_{1-x}Mn_xAs$ layers were grown on a GaAs substrate responsible for tensile strain in the layer plane. As a result, the easy magnetization axis is in the same plane [57]. HPL is known to be circularly polarized in the case of circularly polarized excitation [58]. It allowed using optical pumping of spin-polarized electrons for the study of hole polarization in the FM phase exchange field [59] and thereby estimating its strength. Blue and red dots in Figs 1a and 1b denote the spectral dependence of HPL circular polarization of a PM sample measured at $T = 4$ K and 100 K, respectively. In this experiment, the circularly polarized photons give rise to spin-polarized electrons in the conduction band. Recombination of spin-polarized electrons with equilibrium spin-nonpolarized holes produces circularly polarized HPL photons. Electrons recombining from the birth point do not undergo spin relaxation during their lifetime. Therefore, HPL circular polarization attains its maximum at the high-energy edge. Energy relaxation of electrons to the bottom of the conduction band is accompanied by their spin relaxation, manifested as a reduction in HPL circular polarization with decreasing energy. In a PM sample, circular polarization and its spectral dependence are insensitive to temperature increase within the 4–200 K range, i.e., as long as holes remain bound to the acceptor. Evidently, the spectral dependences of circular polarization measured at $T = 4$ K and 100 K coincide.

The situation changes radically in an ferromagnetic sample. Figure 1b illustrates circular polarization of HPL in the ferromagnetic sample (Curie temperature $T_C = 55$ K) at the same two temperatures. Polarization decreases across the spectrum at the high temperature ($T = 100$ K) as in the paramagnetic sample. A fall in temperature to the liquid

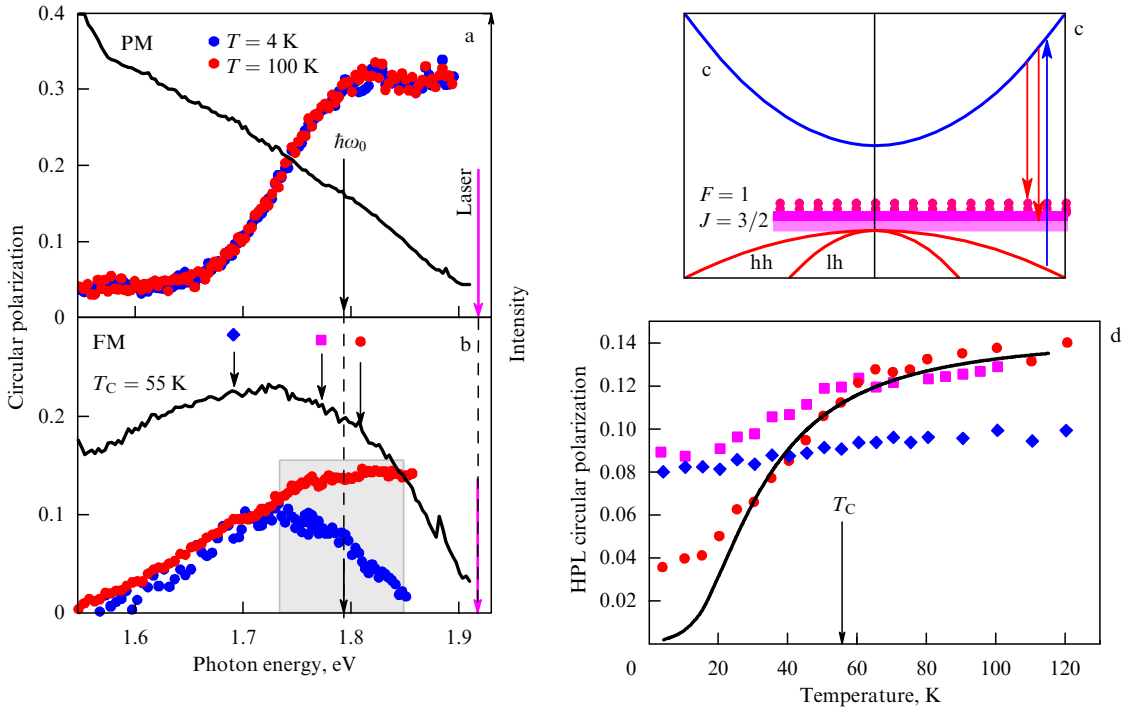

Figure 1. (Color online.) HPL intensity (solid curves) and polarization (symbols) spectra measured for paramagnet (a) and ferromagnet (b) (Ga,Mn)As samples. Polarization spectra measured at two temperatures: $T = 4$ K (blue dots), $T = 100$ K (red dots). Arrows in Fig. b indicate spectral points at which the temperature dependence of circular polarization presented in Fig. d was measured for the ferromagnetic sample. (c) Optical transitions explaining the HPL nature; arrow directed upward — excitation, arrows directed downward — recombination of hot electrons with holes bound on the acceptor or localized in the impurity band, c — conduction band, hh — heavy hole sub-band, lh — light hole sub-band. (d) Temperature dependences of HPL circular polarization measured at spectral points indicated by arrows with respective symbols in Fig. b. Solid curve — calculation.

helium temperature significantly decreases polarization at the highest-energy edge of the spectrum (shaded area in Fig. 1b) and slightly reduces it in the low-energy part of the spectrum. Such polarization behavior is easy to explain taking into consideration that equilibrium hole spin in the FM sample at $T < T_C$ is oriented in the exchange field. In the samples of interest, the easy axis of magnetic anisotropy and the direction of the exchange field lie in the sample plane. At temperatures higher than Curie temperature $T_C = 55$ K, equilibrium hole spins are randomly oriented. Therefore, luminescence due to the recombination of equilibrium holes and electrons having spins oriented along the radiation wave vector acquires circular polarization. At $T < T_C$, hole spins are oriented in the exchange field lying in the sample plane, i.e., normally to the orientation of hot electron spins. Such a geometry implies reduced HPL polarization, which is actually observed at the highest-energy edge of the spectrum.

The different effects of temperature on polarization at high- and low-energy edges of the HPL spectrum can be explained by the superposition of contributions from two types of optical transitions (Fig. 1c) undergoing different polarizations in the exchange field, as clearly seen from the temperature dependences of polarization measured at the three spectral points shown in Fig. 1b. It was calculated in [59] that complete polarization of acceptor-bound holes may cause a 5% reduction in HPL polarization compared to its initial level in the absence of the exchange field. Such a change in polarization occurs at the low-energy edge of the HPL. Polarization of luminescence due to the recombination of spin-polarized electrons with weakly bound holes having a spin of 2/3 can vanish in the exchange field that orients hole spins in the sample plane, i.e., perpendicular to electron spins. The calculations were made on the assumption that a hole with a spin of 2/3 is localized on the weak disorder potential fluctuations. Such states are likely to form in the impurity band from excited Mn acceptor states. The state of such an impurity band was calculated in the zero radius potential model. The temperature dependence of such a transition polarization is shown in Fig. 1d by the solid curve. Clearly, the theoretical dependence fairly well describes the polarization behavior at the high-energy edge of HPL dominated by the contribution to luminescence from weakly bound holes of the impurity band.

The theoretical dependence includes the value of the exchange field or the hole spin splitting value as the fitting parameter. Such fitting allowed the spin splitting value of a weakly bound hole to be estimated at 6 meV, which is equivalent to the exchange field value $B_{\text{eff}} = 90$ T, i.e., significantly lower than that predicted by the mean-field Zener model. For a sample with the comparable Mn content $x = 0.05$ on the assumption of degenerate holes, this model predicts a spin splitting value of 30 meV [42]. On the other hand, the spin splitting value obtained for weakly bound holes proved much higher than the exchange interaction constant in an isolated Mn acceptor equaling 2.3 meV [26]. In other words, weakly bound holes of the impurity band interact with larger number of Mn atoms and therefore experience the influence of a stronger exchange field. Apparently, it is these collectivized holes that induce the ferromagnetic order in (Ga,Mn)As.

2.3 Hot photoluminescence in (Ga,Mn)As under uniaxial static deformation

Let us consider the possibility of controlling HPL magnetization by means of external deformation. As is known, the

magnetic anisotropy of various materials and structures can be controlled by deformation arising during epitaxial growth [60, 61] or by optically induced dynamic strains (see Section 6.2.4). The influence of uniaxial stationary deformation on DFS (Ga,Mn)As magnetization in the external magnetic field was investigated in Ref. [62].

Figure 2 illustrates dependences of HPL circular polarization measured at various external strains perpendicular to the external magnetic field. A comparison of polarization curves measured at different strains shows that saturation ρ^{sat} of HPL polarization (the horizontal dashed line in Fig. 2a) decreases with increasing deformation, while the magnetic field value B_s at which polarization curves are saturated increases. Reduced polarization saturation ρ^{sat} of a doped sample is due to a trivial effect of mixing between sublevels $m_F = 0, \pm 1$ of the Mn acceptor ground state with increasing strain. Analysis of the strain dependence of the saturation magnetic field $B_s^{2/3}(P)$ (Fig. 2b) reveals its nontrivial behavior. This dependence can be represented by two linear functions with different slopes. At the initial stage, a strain dependence of the saturation field with a small slope is observed. The slope sharply increases as deformation exceeds $P \geqslant 2$ kbars. The dependence of the saturation magnetic field B_s on the applied strain P can be expressed as

$$B_s = \begin{cases} 8\sqrt{\dfrac{(K_1 + K_{u1})^3}{6K_1}}\left(1 + \dfrac{b_1}{2(K_1 + K_{u1})} P\right)^{3/2} \\ \text{at} \quad P < P_m\,, \end{cases} \tag{1}$$

$$\begin{cases} 8\sqrt{\dfrac{(K_1 + 2K_{u1} + 2K_{u2})^3}{3K_1}}\left(1 + \dfrac{b_1 + b_2}{K_1 + 2K_{u1} + 2K_{u2}} P\right)^{3/2} \\ \text{at} \quad P > P_m\,, \end{cases} \tag{2}$$

where P_m is given by

$$P_m = \frac{(2^{5/3} - 1)K_1 + 2(2^{2/3} - 1)K_{u1} - 2K_{u2}}{b_2 - (2^{2/3} - 1)b_1}\,, \tag{3}$$

K_1 is the cubic anisotropy constant, K_{u1} is the 'easy axis' type anisotropy constant, K_{u2} is the anisotropy constant taking account of the easy axis in the plane, and b_i are magnetoelastic coefficients. Dependence $B_s^{2/3}(P)$ presented in Fig. 2b can be explained as follows. The application of uniaxial strain orients the magnetization vector along the strain direction and it begins to rotate in plane (P, B) as the magnetic field increases. The dependence shown in Fig. 2b clearly demonstrates a transition from condition (1) to (2). In both samples, this transition occurs at $P_m \approx 2$ kbars. The observed dependence is described in the best way at the following parameters: $K_1 \approx 510$ E cm^{-3}, $K_{u1} \approx 100$ E cm^{-3}, $K_{u2} = -35$ E cm^{-3}, $b_1 \approx 90$ E kbar^{-1}, $b_2 \approx 690$ E kbar^{-1}.

The influence of uniaxial strain on the magnetic properties of (Ga,Mn)As is not reduced to the rotation of the magnetization vector in the direction of deformation alone; it is just as well manifested in the strain dependence of the exchange constant of p–d interaction. It has recently been shown in [63] that, in the case of an isolated Mn acceptor, uniaxial strain causes a 20% decrease in the exchange constant at $P = 5$ kbars. Certainly, this effect should be taken into account in analyzing strain influence on DFS magnetic properties.

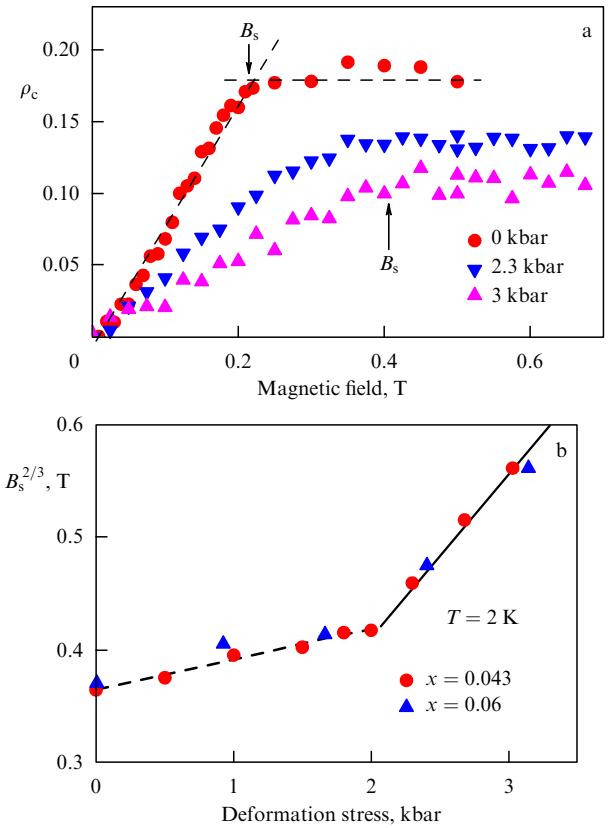

Figure 2. (Color online.) (a) Magnetic field dependences of HPL circular polarization measured in the absence of strain and at uniaxial deformation of $P = 2.3$ kbar and $P = 3$ kbar. The B_s arrow indicates the value of saturating magnetic field. (b) Dependence of $B_s^{2/3}$ on applied uniaxial deformation P. The slopes of dashed and solid lines define two different regimes of magnetization behavior in FM samples with Mn content $x = 0.043$ (dots) and $x = 0.06$ (triangles).

2.4 Spin relaxation in (Ga,Mn)As

The exchange p–d interaction between holes and magnetic ions results in ferromagnetic ordering. The same interaction leads to renormalization of the g-factor of the Mn ion itself and relaxation of its spin. The studies of collective hole-magnetic ion excitations were carried out with the use of such methods as the magnetooptical Kerr effect with time resolution [64–66], ferromagnetic resonance [67, 68], and picosecond acoustics [69].

To reveal mechanisms of Mn spin relaxation in the magnetic semiconductor (Ga,Mn)As and determine its effective g-factor, we used inelastic spin-flip light scattering (ISFLS) [25, 26, 70]. Dependences of the line width and energy shift of the ISFLS line on temperature and the applied magnetic field were evaluated in $Ga_{1-x}Mn_xAs$ samples with Mn atomic fraction $x = 1\%$ ($T_C = 35$ K), $x = 1.4\%$, $x = 4.3\%$ ($T_C = 55$ K). Grey color in Fig. 3a represents the ISFLS spectrum of a doped GaMn:As sample ($p = 10^{18}$ cm^{-3}). The energy shift of the ISFLS line center and its dependence on the applied magnetic field $\Delta = g\mu_B B$ (where μ_B is the Bohr magneton) corresponds to $g = 2$, which allows this line to be related to the transition that corresponds to Mn spin-flip and is split in the external magnetic field. In the doped sample, the width of the ISFLS line and its energy shift in the fixed magnetic field are independent of temperature.

In a paramagnetic DMS (purple curve in Fig. 3a), the ISFLS line is markedly broadened, but neither its width

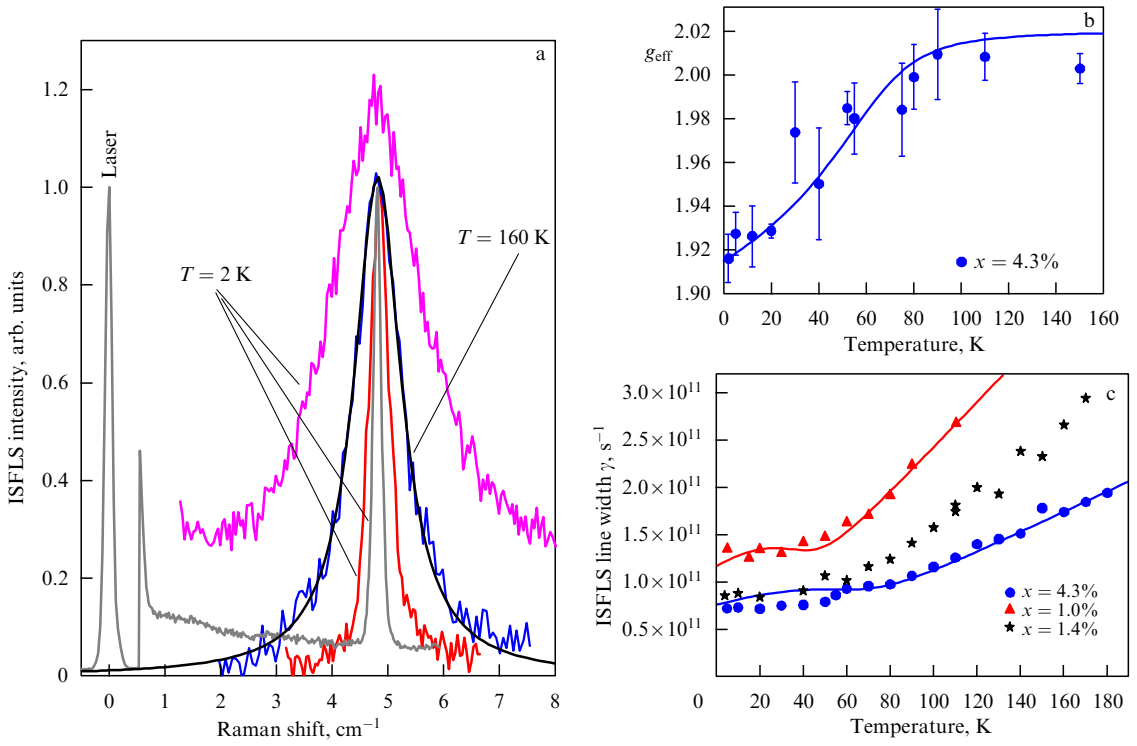

Figure 3. (Color online.) (a) ISFLS spectra measured for doped GaAs:Mn (Mn concentration 10^{18} cm^{-3}) in PM ($x = 0.008$) and FM ($x = 0.043$) samples at temperatures $T = 2$ K and $T = 160$ K. (b) Temperature dependence of Mn g-factor measured for FM sample ($x = 0.043$). (c) Temperature dependence of ISFLS line measured for samples with $x = 0.01$, $x = 0.014$, and $x = 0.043$. Solid curves are the result of approximation of experimental data using expression (5).

nor energy shift shows temperature dependence. On the contrary, both the width of this line and its energy shift in a ferromagnetic DMS are temperature-dependent (cf. spectra at $T = 4$ K (red line in Fig. 3a) and $T = 160$ K (blue line in Fig. 3a)). The absence of magnetic field dependence of the line width allows concluding that the ISFLS line width is related to Mn transverse spin relaxation measured in the temperature range from 2 to 200 K for three samples (Fig. 3c).

Modification of the Mn g-factor and its transverse spin relaxation time was described based on the concept of two magnetic subsystems consisting of an ensemble of holes and Mn ions. As is known, there is no direct interaction between Mn centers in (Ga,Mn)As and ferromagnetism is due to the presence of holes [71]. The rigorous microscopic theory describing the nature of ferromagnetism in such systems is still absent [71]. We have proposed a phenomenological description of the Mn ion spin behavior in the strongly correlated spin system being investigated. Magnetization fields of these subsystems were introduced for this purpose to describe the spin dynamics of the ensemble of Mn holes and ions [72]. We assumed the presence of exchange interaction between two magnetic subsystems, hole spin diffusion, and hole spin relaxation, due to the strong spin-orbit interaction in the GaAs valence band, and took into account the spin waves in this system. This assumption allows the effective g-factor g_{eff} and the transverse spin relaxation rate γ of Mn to be presented as [70]

$$g_{\text{eff}}(T) \approx g_S - (g_S - g_J)\,\frac{\lambda_S M_J^0(\lambda_J M_S^0 + \lambda_S M_J^0)}{(\lambda_J M_S^0 + \lambda_S M_J^0)^2 + \gamma_{\text{h}}^2}\,, \qquad (4)$$

$$\gamma(T) \approx \frac{T\lambda_S^2}{(2\pi)^2(D\sqrt{\alpha_J C_J} + C_J\sqrt{D\gamma_{\text{h}}})} + \gamma_{\text{h}}\,\frac{\lambda_S M_J^0(\lambda_J M_S^0 + \lambda_S M_J^0)}{(\lambda_J M_S^0 + \lambda_S M_J^0)^2 + \gamma_{\text{h}}^2}\,, \qquad (5)$$

where M_S and M_J are magnetizations of Mn spin subsystems and holes (the latter can be neglected) [71], $\lambda_S = \lambda g_S \mu_{\text{B}}/\hbar$ and $\lambda_J = \lambda g_J \mu_{\text{B}}/\hbar$ describe interaction between spin subsystems, D is the hole spin diffusion coefficient, γ_{h} is the hole spin relaxation rate, and $C_J = (C_1 C_2 - C_3^2)/C_1$. Here, C_i are constants describing the energy spectrum of spin waves of holes (C_2), Mn ions (C_1), and the collective mode (C_3).

In this concept, the effective g-factor defines the frequency of the collective precession mode of the system [72]. To describe Mn g-factor modification, linearized equations of motion can be considered on the assumption of a small deviation in magnetization from equilibrium. The parameter determining temperature dependence of the g-factor is the mean magnetization in the system. Based on this assumption, we evaluated the temperature dependence of the effective g-factor of Mn centers (4). There was no renormalization of the g-factor at temperatures above the Curie point due to the absence of a mean magnetic moment in the system (Fig. 3b).

An analysis of Eqns (4), (5) revealed two hole-related contributions during spin relaxation (5) (Fig. 3c). At temperatures below T_{C}, rapid spin relaxation of the holes is associated with spin-orbit interaction in the valence band of gallium arsenide. Hole spin relaxation causes relaxation of Mn ion spins due to collective motion of subsystems consisting of Mn ions and the ensemble of holes. The implementation of this mechanism requires the presence of

the mean magnetic moment. Therefore, it plays a key role at temperatures below T_C. Another mechanism is underlain by spin fluctuations of the hole subsystem giving rise to an effective magnetic field acting on the Mn ion spin. This mechanism operates over the entire temperature range but prevails at $T > T_C$. It was found by comparing theoretical and experimental dependences of transverse Mn ion spin relaxation times that the hole spin relaxation time of the (Ga,Mn)As ferromagnet equals 0.9 ps and the characteristic time of Mn ion spin relaxation is 30 ps.

In conclusion, we note that the use of optical methods for the study of DFS made it possible to obtain important information on the mechanisms of spin relaxation in Mg ions and the exchange renormalization of its g-factor. Our studies also revealed highly heterogeneous magnetic properties of (Ga,Mn)As, as confirmed by the co-existence of FM and PM phases in a nominally ferromagnetic sample. Detailed analysis of polarization characteristics of the HPL allows the conclusion that ferromagnetism is due to delocalized holes of the impurity band. Finally, we demonstrated the possibility of controlling the magnetization vector using uniaxial strain.

3. Ferromagnetic proximity effect in a hybrid ferromagnet-semiconductor structure

The strategy of magnetism integration into semiconductor electronics alternative to DMS creation is based on a combination of ferromagnetic and semiconductor (SC) materials within a single heterostructure. In such hybrid FM/SC structures, each component retains its main properties without worsening those of the other component, namely the high mobility of charge carriers in SC and magnetic characteristics of FM structures [73].

A key issue is the choice of the optimal FM/SC combination from a variety of potential materials for the purpose. One of the concepts of hybrid FM/SC structures gives priority to the injection of spin-oriented charge carriers from FM into SC structures [1]. Spin polarization efficiency of charge carriers in SC structures can amount to 50% [35] even if it is likely to reduce due to the large difference between electric conductivities of FM and SC structures. Another concept is based on the p–d exchange interaction between magnetic atoms in the FM and holes in the SC quantum well. This interaction induces the ferromagnetic proximity effect, i.e., equilibrium hole spin polarization, which, in turn, influences the orientation of magnetization [74]. The composite spin system of FM/SC is flexible, since it allows optical and electric control of its magnetic anisotropy.

Historically, the FM/SC proximity effect was observed for the first time in a hybrid Ni/GaAs ferromagnetic/bulk semiconductor structure [75, 76]. Ni diffusion into GaAs creates a magnetic NiGaAs interface whose important feature is the photocoercivity effect, i.e., optical rearrangement of its coercivity field [77, 78]. Photocoercivity is due to the influence of the GaAs semiconductor on the ferromagnetic interface, which decreases if the photon energy is lower than GaAs bandgap. Thus the electron exchange interaction in the NiGaAs interface is controlled by GaAs optical excitation.

Modern nanotechnologies allow creating FM/SC heterointerfaces, parts of which can be controlled with nanometer accuracy. The search for an ideal heteropair for hybrid FM/SC structures includes solving two main problems: (1) polarization of charge carrier spins in a quantum well (QW) and (2) electrical control of ferromagnetism through spin-polarized charge carriers. At present, only the first task has been accomplished: spin polarization in SC-quantum wells generates circularly polarized luminescence [79–81].

The uniqueness of FM/SC structures is due to the combination of magnetism and the possibility of controlling the concentration of charge carriers in the semiconductor, making possible electric control of magnetism in a composite system, the key issue being the distance over which spin-spin interactions can propagate from the ferromagnet to the semiconductor, because it determines the functional potential of a device based on such hybrid structures.

The exchange interaction due to overlapping wave functions is the strongest one, but it is short-range. Nevertheless, Ref. [81] reports, for a heterostructure with the Co layer spaced ~ 10 nm from the CdTe (Co/CdMgTe/CdTe/CdMgTe superconductor quantum well, the effective long-range interaction unrestricted by wave function overlap. The authors hypothesize that the interaction is implemented through transverse acoustic oscillations of the crystal lattice elliptically polarized near the magnon-phonon resonance. In Sections 3.1–3.3, we consider ongoing research on spin-spin interactions in FM/SC interface structures.

3.1 Equilibrium proximity effect. Hole gas polarization in the ferromagnetic exchange field

Reference [74] proposes a concept of the ferromagnetic proximity effect, i.e., strong coupling of ferromagnetic spins with spins of charge carriers of a nonmagnetic semiconductor near the FM/SC QW interface (Fig. 4). A ferromagnetic film with magnetization **M** is coated on an SC heterostructure consisting of a QW separated by barriers from the FM film above and a nonmagnetic metal beneath. The metallic nonmagnetic valve at the top is intended to control the concentration of holes in the QW. In the absence of magnetic

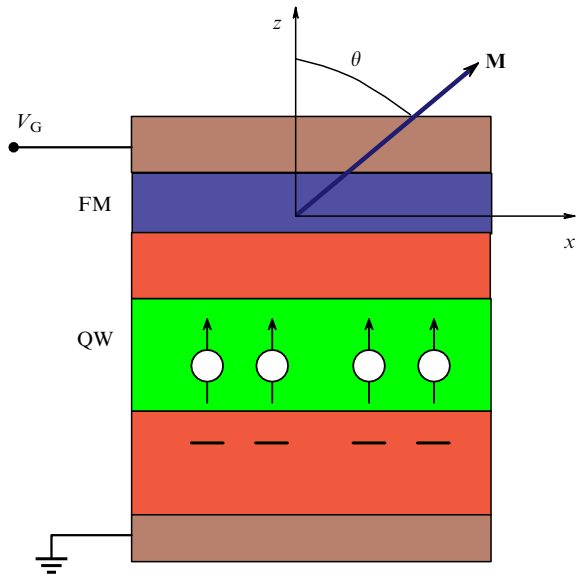

Figure 4. (Color online.) Schematic diagram of a structure whose operation based on the proximity effect. A semitransparent barrier separates the ferromagnet (FM) from the quantum well (QW), which, in turn, is separated by a barrier from nonmagnetic metallic contact. Metal valve at the top of the structure serves to control hole concentration in the QW. Arrows in the QW indicate hole spin orientation [74].

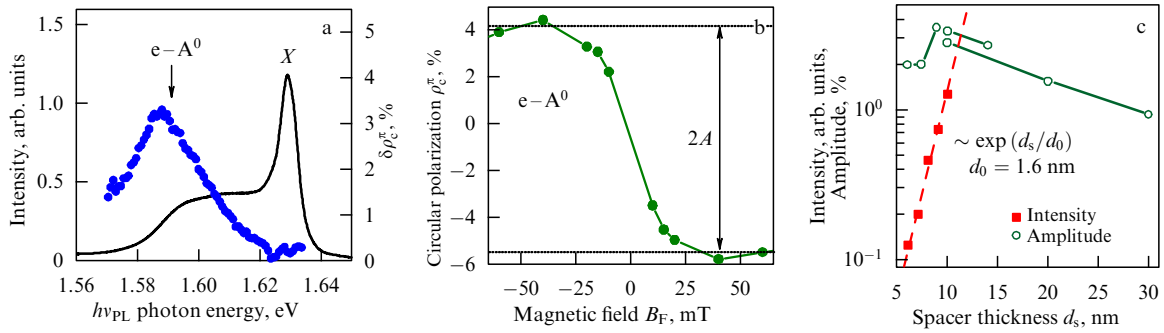

Figure 5. (Color online.) Long-range equilibrium proximity effect. (a) Spectral dependence of PL intensity and induced circular polarization $\delta\rho_c^\pi(B_F) = [\rho_c^\pi(+B_F) - \rho_c^\pi(-B_F)]/2$ for linearly polarized excitation in magnetic fields $B_F = \pm 10$ mT at $T = 2$ K in a hybrid Co/(Cd,Mg)Te/CdTe/(Cd,Mg)Te structure. (b) Dependence $\rho_c^\pi(B_F)$ measured for e–A^0 transition as shown by vertical arrow in Fig. a. (c) Dependence of intensity of PL from a QW on spacer thickness d_s (red squares). Dashed line is the result of fitting using the formula $\exp(d_s/d_0)$ with characteristic length $d_0 = 1.6$ nm. Unfilled green circles show dependence of proximity effect amplitude A on thickness d_s. (From [81].)

interaction between the quantum well holes and magnetic atoms of the FM film, the direction of easy magnetization in the latter coincides with the x-axis.

It is also supposed that the spin-orbit splitting of heavy and light holes is great and, therefore, the hole spin in a QW is strongly coupled to the direction of the normal. In the case of an impenetrable barrier between the FM film and the QW, the FM and QW systems are uncoupled, with FM magnetization lying in the structure plane parallel to the x-axis, whereas the hole gas in the QW is spin-nonpolarized in the absence of an external magnetic field. However, in the presence of a semipermeable barrier, the wave functions of heavy holes and FM magnetic atoms overlap, and exchange interaction between holes and magnetic atoms takes place. Since the hole spin is rigidly tied to the normal, this interaction is proportional to the product of z-components of the hole spin and vector **M**. Spontaneous spin-polarization of the holes becomes an advantage as exchange increases. The polarized holes, in turn, rotate vector **M** from the plane toward the direction of the normal (see Fig. 4). Feeding electric displacement to the top electrode attracts holes to or repulses them from the ferromagnet, thereby increasing or reducing FM/SC exchange coupling. Thus, the interface spin-spin interaction creates a unified spin system, the properties of which are significantly different from the properties of an isolated FM film.

The uniqueness of the FM/SC system consist in the electrical controlling of nonmagnetic SC properties, allowing a semiconductor not only to serve as a passive substrate for a ferromagnet but also to actively participate in information processing. Spin polarization in QWs induced by Mn ions in (Ga,Mn)As was electrically detected by the anomalous Hall effect [82]. The proximity effect was also found in similar structures by observing the circular polarization of exciton fluorescence from the QWs [79, 80]. In the latter case, however, an alternative mechanism responsible for the dynamic proximity effect due to spin-dependent capture of electrons from the QW into the ferromagnet is possible [83] (see Section 3.3).

3.2 Long-range equilibrium proximity effect. Indirect ferromagnet-semiconductor exchange via elliptically polarized phonons

A recent paper [81] reports the equilibrium proximity effect in the FM/QW heterostructure Co/(Cd,Mg)Te/CdTe/(Cd,Mg)Te containing group II–VI semiconducting materials. The proximity effect begins to manifest itself in very weak longitudinal magnetic fields $B_F = 10$ mT (Fig. 5). It is expressed in ferromagnetic-induced circular polarization of photoluminescence (PL) developing as a result of radiative recombination of conduction-band electrons with acceptor-bound holes in a QW (e–A^0 transition). Figure 5 shows the dependence of circular polarization ρ_c^π on the magnetic field, which is saturated at $B_F \approx 40$ mT with the effect amplitude $A \approx 4\%$, i.e., one order of magnitude higher than in the absence of the Co layer.

Measurement of the PL dynamics and its polarization with time resolution showed that acceptor-bound holes in QW acquire polarization as a result of efficient p–d exchange with Co atoms. Surprisingly, this effect proved to be a long-range one unrelated to overlapping wave functions of charge carriers in QWs and magnetic atoms in ferromagnets (Fig. 5c). It was suggested that the long-range exchange interaction can be due to the influence of elliptically polarized phonons on the acceptor spin levels in QWs (Fig. 6).

A circularly polarized phonon with energy $\hbar\omega_q > \Delta_{lh}$ couples the $+3/2$ state of a heavy hole to the excited $+1/2$ state of a light hole by inducing the spin-dependent shift of spin hole levels. This effect is a phonon analog of the dynamic optical Stark effect or the inverse Faraday effect taking place in the case of irradiation by elliptically polarized light in the transparency band.

The presence of polarized phonons in the FM layer is due to the phonon–magnon interaction responsible for the strong circular dichroism of the former. There is no appreciable potential barrier for phonons at the border between the FM layer and the QW in a hybrid structure, in contrast to the potential barrier that hampers tunneling of charge carriers. Thus, phonons with circular polarization determined by FM magnetization can relatively freely penetrate into the QW and interact with charge carriers. Characteristic frequencies of these elliptically polarized phonons (~ 1 meV) are close to energy splitting between heavy ($|\pm 3/2\rangle$) and light ($|\pm 1/2\rangle$) holes localized on acceptors in the QW (a quasi-resonance case). Spin–phonon interaction removes Kramers degeneracy of the $|\pm 3/2\rangle$ doublet in a zero external magnetic field. The ~ 0.1 meV exchange splitting of $|\pm 3/2\rangle$ acceptor spin levels in QWs was measured directly by the inelastic spin-flip light scattering technique [84].

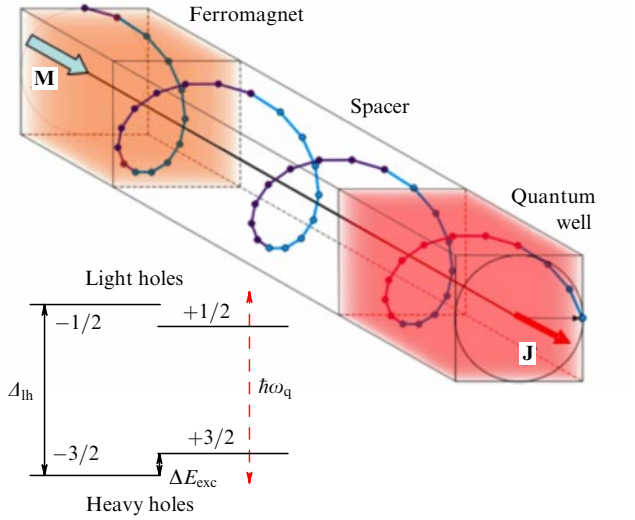

Figure 6. (Color online.) Illustration of circularly polarized phonon mode in a hybrid FM-QW structure and energy diagram of hole levels on an acceptor in the QW.

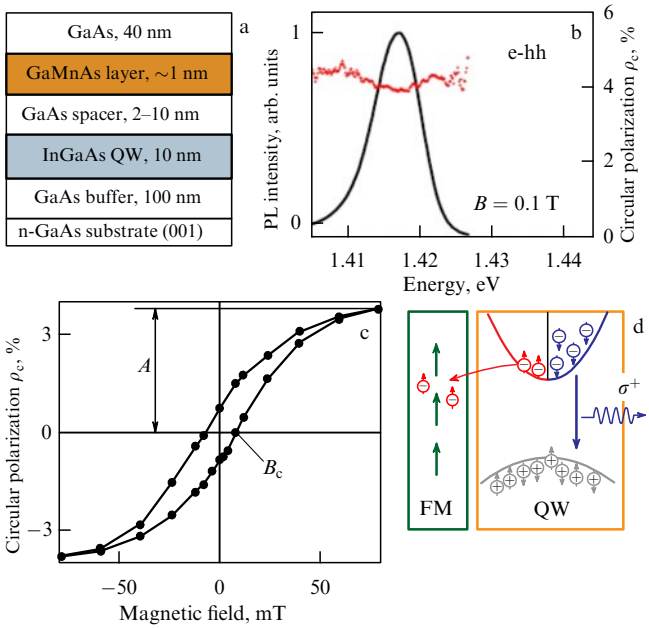

Figure 7. (Color online.) Dynamic proximity effect. (a) Structure diagram. (b) PL intensity (black curve) and polarization (red dots) spectra for a sample with 10-nm-thick spacer in the case of linearly polarized excitation with a photon energy of 1.92 eV and power 2 mW at $T = 2$ K. (c) Polarization hysteresis loop $\rho_c^{\pi}(B)$ in the Faraday geometry for e−hh transition; B_c is the coercitive force, amplitude $A \equiv \rho_c^{\pi}(B_F = 80$ mT). (d) Illustration of spin-dependent electron capture and spin accumulation.

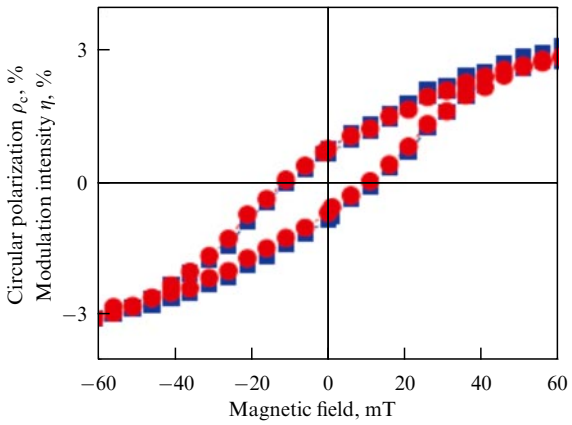

Figure 8. (Color online.) Magnetic dependences of PL polarization $\rho_c(B)$ and integral intensity modulation parameter $\eta(B_F)$ measured upon light-induced excitation with polarization and detection of total PL intensity at the exciton recombination line.

3.3 Dynamic proximity effect. Electron polarization in spin-dependent capture of electrons from a quantum well by a ferromagnet

Let us consider the dynamic nonequilibrium proximity effect due to spin-dependent capture of electrons from a QW into FM. Tunneling of charge carrier spin levels from a QW into FM, besides their splitting in the QW (see Section 3.2), leads to the broadening of the levels due to the finite lifetime in the QW. This broadening is spin-dependent, because it is conditioned by different probabilities of the tunneling of charge carriers with spins oriented along and against the magnetization direction in FM. The dynamic effect was observed in hybrid structures consisting of the (Ga,Mn)As FM layer separated from the QW (In,Ga)As by a 2–10-nm-thick GaAs spacer [83] (Fig. 7a). The spin-dependent escape of electrons into FM leads to their dynamic spin polarization (Fig. 7d) due to the accumulation of electrons with spin projection corresponding to slower tunneling in the QW. As a result, the exciton PL intensity spectrum (the e-hh line), shown by the black curve in Fig. 7b, turns out to be circularly polarized (red dots in Fig. 7b). The dependence of circular polarization degree of PL from the QW on the magnetic field demonstrates hysteresis (Fig. 7c) as a consequence of FM perpendicular magnetic anisotropy.

The main argument in favor of this effect being caused by spin-dependent capture is the dependence of integral intensity of the PL from the QW on circular polarization of excited light that generates electrons with the spin oriented along or against the magnetization direction. This fact is revealed by measuring the modulation parameter $\eta = (I^+ - I^-)/(I^+ + I^-)$ defined as the relative difference between total intensities I^+ and I^- of PL excited by σ^+- and σ^--polarized light, respectively. Circular polarization ρ_c^{π} corresponds to the relative difference between σ^+- and σ^--intensities of the PL excited by linearly polarized light. It was shown in experiment that the degree of PL intensity modulation (blue squares in Fig. 8) coincides with polarization dependence ρ_c^{π} (red dots in Fig. 8).

When the mechanism of equilibrium hole polarization in the FM exchange field predominates, the spin-dependent capture is inessential and the modulation parameter is negligibly small. The proposed method permits studying both FM/QW exchange interaction effects and spin-dependent tunneling of carriers from the QW into FM.

Investigations into the optical and magnetic properties of hybrid systems based on the QW and FM layer give evidence of the multiplicity of possible mechanisms underlying the proximity effect, including short-range exchange due to wave function overlap, the spin-dependent capture of carriers from the quantum well into ferromagnetic, or long-range interaction via circularly polarized phonons. The proximity effect permits determining the ferromagnet magnetization state by measuring the polarization of the PL from the nonmagnetic

QW. The next step toward integration of magnetism into semiconductor electronics is elucidation of the possibility of controlling exchange interaction by means of the external electric field.

4. From manipulation of spin ensembles to single spin manipulations under ambient conditions

Coherent manipulations of single spins in solids under ambient conditions attract much attention in view of the great perspectives for their application in technologies of atomic-scale devices, including fundamentally new protocols of quantum information processing and probing various physical fields with nanometer spatial resolution [85]. In this context, spins are of special interest due to relatively long coherence times.

It was shown that the magnetic moment associated with individual quantum systems can be detected by transport measurements with single quantum dots [86] and defects in silicon [87]. Magnetic resonance force microscopy also attained the sensitivity limit [88]. However, most attention has been given (especially in recent years) to the development of optical methods for detecting magnetic resonance of single spin centers. The optically detected magnetic resonance (ODMR) technique using a single spin center opened up promising prospects for the combination of highly sensitive optical microscopy and conventional magnetic resonance technology.

After the discovery of a single molecular spin [89, 90] quantum states associated with single defects in diamonds were studied [91]. Experiments with isolated nitrogen-vacancy (NV) defects in diamond are especially interesting in view of the long coherence time for color center spins that allows a single spin to be detected and coherently controlled in a solid at room temperature, and thereby provides a basis for new quantum technologies.

Later studies revealed families of homotypic color centers in silicon carbide with $S = 1$ and $S = 3/2$ possessing unique spin properties [92–102]. The optically induced alignment (polarization) of spin sublevels in ground and excited states of color centers in families with $S = 3/2$ has been observed in various SiC polytypes (4H-, 6H-, and 15R-SiC) at room temperature. Two opposite scenarios of optical alignment of centers with $S = 3/2$ were implemented in such systems, in which optical pumping populates either upper or lower levels, depending on crystal polytype, temperature, and spin center structure. Observed Rabi nutations persist for about 100 μs at room temperature, which implies that the spin ensemble can be obtained in the coherent superposition of spin states in resonant magnetic fields at room temperature.

A four-level system with $S = 3/2$ can be regarded as a double qubit functioning at room temperature. Electron spins can be manipulated by applying a 1–200 MHz radiofrequency (RF) field compatible with nuclear magnetic resonance frequencies. The emphasis is laid on color centers exhibiting optical activity in the near infrared (IR) spectral region preferable for potential *in vivo* biological applications owing to deep penetration into living tissues and consistency with fiber optics technology. The probing concept is based on variants of the ODMR method and such physical effects as optical response to anticrossing or cross-relaxation of energetic spin levels with high sensitivity, up to the sensitivity to single spins [100–102].

Optically-induced inversion of spin state population even in zero magnetic fields gives rise to induced microwave radiation that can be used to construct solid-state masers and highly sensitive radiofrequency amplifiers as well as for recording microwave radiation at certain frequencies in outer space, keeping in mind that silicon carbide (carborundum) has been found in space objects (meteorites). The possibility of performing high-temperature spin manipulations eliminates temperature limitations on spin processes in animate nature, including the use of quantum calculations for modeling the human nervous system.

As a result, single photon sources were created and the possibility of quantum manipulations with single electron and nuclear spins was realized, nanoscale magnetic probing with the use of individual electron spins was carried out, and single defect radiation was introduced into near-field optical microscopy. The search for new systems as sources of single photons in the optical range to be employed in various applications is also a priority area of ongoing research.

Experiments on studying isolated quantum systems in solids have contributed to a better understanding of the dynamics and energy structure of the respective materials and quantum optical processes associated with light-matter interaction. Unlike early experiments with single atoms in atomic systems, modern studies with the use of impurity atoms in solids encounter difficulties, because most single quantum systems in solid matter strongly interact with their environment. First of all, single solid quantum systems are embedded in the surrounding medium that scatters excitation light. It can be argued, taking into account the diffraction-limited focal volume, that the number of matrix atoms is usually $10^6 - 10^8$ times that of the quantum systems being considered, imposing an upper limit on impurity content in the matrix.

An analysis of various systems, such as single hydrocarbon molecules, proteins, quantum dots, and defect centers, was undertaken [103]. Single quantum systems were detected by photoluminescence techniques in which an optically-excited state was pumped with the use of an excitation laser in resonance with the highly resolved optical transition of the system.

Figure 9a presents a simplified three-level diagram describing the optical excitation/emission cycle in color centers (e.g., the NV center where ^{3}A and ^{3}E are triplet ground and excited states, respectively, ^{1}A is the metastable singlet state). The figure shows intersystem (IS) transitions and their rates k_{ij}. The solid line corresponds to allowed optical transitions between the ground and excited states; radiationless transitions are indicated by the dashed lines.

Depending on the photoluminescence quantum yield, the system decays either under the effect of the fluorescence radiation, or without it, via IS transitions to a metastable state (^{1}A in the case of NV). In this case, the maximum fluorescence intensity is expressed as

$$I_{\max} = \frac{k_{31}(k_{21} + k_{23})\Phi}{2k_{31} + k_{23}} . \qquad (6)$$

Here, k_{31} is the rate of radiationless transition from the metastable to the ground state, k_{21} is the rate of radiative transition from the excited to the ground state, k_{23} is the rate of radiationless transition to the metastable state, and Φ is the fluorescence quantum yield.

The PL intensity $I_{\max}$ for the NV center is roughly 10^7 photons per second, while $I_{\max}$ critically depends on several parameters. First of all, the fluorescence quantum yield restricts maximum radiation. The highest photon

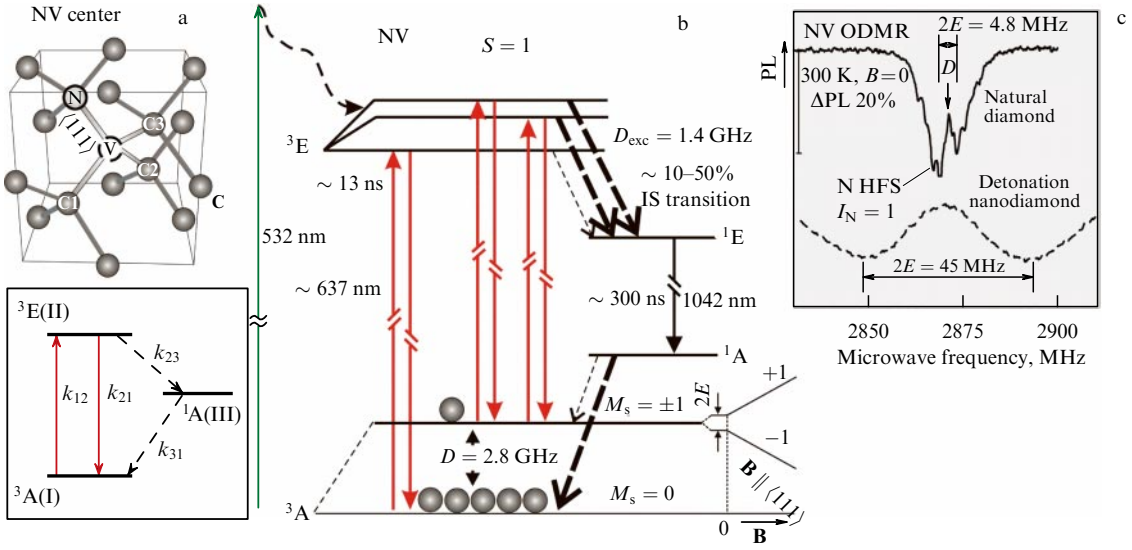

Figure 9. (a) Simplified three-level diagram describing the cycle of optical excitation and radiation of an ensemble or an isolated NV center with the structure shown in the top left part of the figure. Arrows and k_{ij} denote rates of transitions between different states. (b) Detailed diagram of NV center energy levels; allowed optical transitions between triplet ground and excited states are shown by solid line. Nonradiative transitions are denoted by dashed lines. Arrow thickness reflects intensity of spin-dependent intersystem transitions. (c) ISFLS spectra in a zero magnetic field.

radiation from an NV center is 10^5 s^{-1}. Figure 9b presents a more detailed NV recombination scheme showing the way to the optical alignment of the population of the lower level with $M_S = 0$ of the ground state. PL intensity I_{max} depends on the spin state via the rate k_{23}. A change in the spin state (e.g., in the case of magnetic resonance) leads to a more than three orders of magnitude variation of this rate (a few kHz to several MHz). This accounts for the pronounced (up to 30%) alteration of PL intensity.

The Hamiltonian describing energy levels in the triplet spin state shown in Fig. 9 has the form

$$H = g\mu_B \mathbf{SB} + D\left[S_z - \frac{1}{3}S(S+1)\right] + E(S_x^2 - S_y^2) + \mathbf{S}A_N\mathbf{I}_N + \mathbf{I}_N Q_N \mathbf{I}_N ,$$

where g is the electron g-factor of NV defect, μ_B is the Bohr magneton, $\mathbf{S}$, S_z^2, S_x^2, and S_y^2 are operators of electron spin and respective projections, $S = 1$, D and E are parameters of fine structure splitting, $\mathbf{I}_N$ is the nuclear spin operator, A_N is the tensor of hyperfine interaction with nitrogen nucleus, and Q_N is the tensor of quadrupole interaction with the nitrogen nucleus.

The first term on the right-hand side of the Hamiltonian describes Zeeman levels in the magnetic field for the triplet spin state, the second and third ones describe the fine structure independent of the magnetic field, while the last two describe hyperfine and quadrupole interactions that are also independent of the magnetic field. The typical ODMR spectra for NV centers in a zero magnetic field are presented in Fig. 9c. It is important that the parameter E related to internal stresses in a crystal leads to the splitting of ODMR spectra and the appearance of an additional hyperfine structure (HFS) caused by nitrogen nuclei. For comparison, the figure shows schematically the splitting observed in a detonation nanodiamond that is an order of magnitude greater than in natural diamonds.

Single color centers in diamond and silicon carbide can be observed by standard confocal and fluorescent microscopy. In confocal microscopy, a laser beam is focused into a diffraction-limited spot in diamond or silicon carbide samples, and fluorescence is gathered from this spot. This means that the focal probe volume is diffraction-limited by roughly 1 μm^3 in size. It is important to control defect density in order to detect separate centers. For NV centers and color centers in SiC, such control is performed by varying the number of vacancies created in the sample, e.g., by selecting proper electron irradiation doses. The number of NV centers also depends on the number of available vacancies and nitrogen atoms in the sample.

Figure 10a shows, as an example, a series of PL spectra for different powers of exciting light with a wavelength of 760 nm and a confocal fluorescence image of color centers in an SiC crystal exposed to low-dose electron irradiation ($\sim 10^{12}$ cm^{-2}) where the number of defects is sufficiently small to detect the fluorescence from a single color center. Figure 10d illustrates a reduction in PL at 300 K, corresponding to the lifetime of 6.1 ns in the excited state. As was expected, the image shows diffraction-limited spots. The image provides no information on whether fluorescence is associated with a single quantum system (a single defect) or produced by an aggregate of defects. The number of independent emitters in the focal volume can be estimated based on the statistical distribution of color center fluorescence. The statistical distribution of the number of fluorescent photons in a single two-level quantum-mechanical system differs from the classical Poisson distribution. The fluorescence intensity autocorrelation function has the form

$$g^2(\tau) = \frac{\langle I(t)I(t+\tau)\rangle}{\langle I(t)\rangle^2} , \qquad (7)$$

where τ is the small delay between two photon propagation paths to the detector. For the emission from a single quantum-mechanical system this function is characterized by the value $g^2(0) = 0$.

Figure 10c presents the autocorrelation function of PL intensity of a single color center in SiC at room temperature.

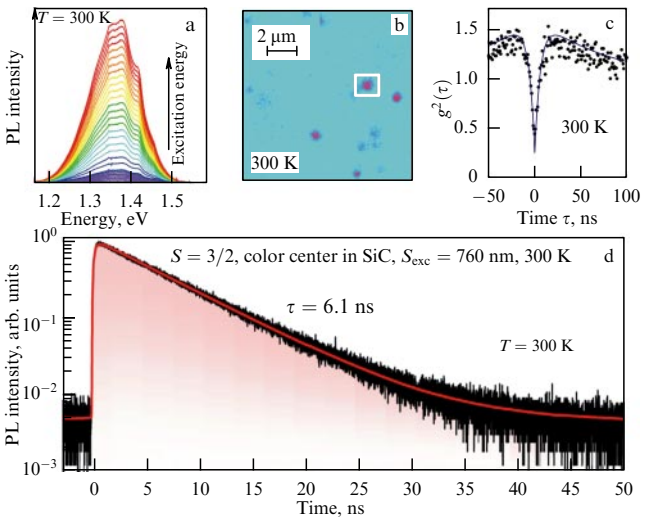

Figure 10. (Color online.) (a) Series of PL spectra at different exciting light powers (760 nm). (b) Confocal fluorescent image of PL color centers in SiC obtained in a crystal exposed to low-dose electron irradiation. (c) Autocorrelation function of PL intensity of a single color center in SiC at room temperature. (d) PL decay at 300 K corresponding to the lifetime of 6.1 ns in the excited state.

The equality $g^2(0) = 0$ arises from the fact that a defect must be excited to enable it to emit one photon, meaning that a single defect never emits two photons at a time, whereas excitation of a random number of independent emitters can induce the emission of several photons. Considering a three-level system, e.g., for NV center (see Fig. 9), it is possible to derive rate equations for time-dependent changes in the populations of all three levels. The solution of the equations reproduces a dip in the correlation function $g^2(\tau)$ at $\tau \to 0$, which indicates that light is radiated from a single NV center. The qualitatively identical expression can be obtained for silicon carbide with the curve slope around $\tau = 0$ determined by the laser pumping rate k_{12} and the emission rate k_{21}. At longer τ, the decay of the correlation function becomes appreciable due to intersystem transitions from the excited to the metastable state.

The emission rate k_{21} depends on the ambient refractive index as $1/n$, where $n = 2.42$ for diamond and $n \sim 2.65$ for silicon carbide. The emission rate k_{21} must increase significantly with decreasing ambient refractive index. Such a relationship actually takes place for the color centers in appropriate nanocrystals. Also promising is the use of metamaterials to control radiative and spin properties of color centers.

Results of statistical measurements of emitted photons also allow conclusions about photoionization and photochromism of isolated NV centers. An NV center exists in two charge states: the negatively charged NV^- center (6 electrons, $S = 1$) with a 637-nm zero photon line and the neutral NV^0 center (5 electrons, $S = 1/2$) with a 575-nm zero photon line. To observe charge transfer from NV^- to NV^0, statistical measurements of photons were carried out, analogous to those for a single-photon radiator. The proper adjustment of the two channels makes possible the detection of radiation from the NV^0 center in one arm of the detector and that from the NV^- center in the other. For delay time $\tau = 0$, the correlation function $g^2(\tau)$ exhibits a dip. It was concluded that the two spectral positions undergo continuous interconversion, namely the photoinduced switching from NV^0 to NV^- takes place, whereas the reverse process ($NV^- \to NV^0$) occurs in the dark with the time constant ranging from 0.3 to 3.6 μs.

In ultrapure diamonds with a low concentration of nitrogen impurities, the low-temperature width of the PL line tends to a limit imposed by the excited state lifetime alone, i.e., having the order of a few dozen MHz. As a result, the width of the optical transition line is much smaller than the splitting of the 2.8-GHz fine structure for the NV center. This opens up possibilities for manipulating spin states and their readout by optical spectroscopy. Spin-orbit coupling leads to spin state mixing in the excited states. As a result, one of the sublevels of the excited state forms a lambda scheme with two spin sublevels of the ground state. The lambda-type transition permits observing electromagnetically-induced transparency [104], nondestructive readout of the spin state [105], and quantum entanglement of photon and spin states [106], which is of utmost importance for the application of NV centers in quantum communication.

The remarkable photophysical properties of color centers provide the possibility of spin readout and manipulation. The combination of optical reading and conventional magnetic resonance makes possible reliable control over the state of single spins. This approach, together with the use of an ultrasensitive optical system, provides a basis for single-spin control. Optical transitions between ground and excited states under ambient conditions are markedly broadened, which makes impossible the spectral choice of selected spin sublevels. However, spin sublevels with the magnetic quantum number $M_S = \pm 1$ have higher probabilities for intersystem transitions into metastable singlet states by virtue of spin-orbit coupling. As a result, fluorescent radiation of an NV center is more pronounced for the spin sublevel with $M_S = 0$. Moreover, intersystem transitions allow an effective spin polarization as a consequence of spin-selective decay of the metastable singlet state into sublevel $M_S = 0$ of the ground triplet state (see Fig. 1).

The low content of ^{13}C and ^{29}Si isotopes with nuclear magnetic moments in diamond and silicon carbide accounts for the long coherence time in these materials. It has been shown that nuclear spins of ^{13}C and ^{29}Si may be regarded as a resource for quantum information protocols. Hyperfine interaction between electron and nuclear spins makes possible the realization of double and triple qubit quantum gates. Obviously, manipulations of isotope composition in these materials are possible for obtaining high coherence properties of spin color centers by decreasing ^{13}C and ^{29}Si concentrations, on the one hand, or increasing them in the case of hyperfine interaction for controlling electron and nuclear spins, on the other hand. Importantly, ^{13}C and ^{29}Si ($I = 1/2$) have nuclear moments of opposite signs, despite the equality of their nuclear spins and close absolute values of nuclear moments; in other words, the nuclear moments precess in opposite directions in a magnetic field. This effect is of interest for designing ^{13}C- and ^{29}Si-based gyroscopes, because it allows using compensation schemes as in xenon isotope-based gyroscopes.

Optical pumping of spin color centers in magnetic fields corresponding to anticrossing of spin levels in the excited state leads to dynamic polarization of single nuclear spins at room temperature. A high-efficiency method for single nuclear spin polarization based on the optical pumping of an isolated NV center in the region of spin level anticrossing in the excited state of the NV defect was demonstrated in

diamond (see [102] and references therein). Nuclear spin polarization in excess of 98% was achieved at room temperature for the ^{15}N nucleus of the NV center, which corresponds to an effective spin temperature on the order of several μK. Also, the possibility of simultaneous polarization of two nuclear spins (^{15}N and ^{13}C) in the vicinity of the NV center was demonstrated. Such reliable control of nuclear-spin states is the key component for the further expansion of quantum registers based on the nuclear spin in diamond and silicon carbide.

Future progress critically depends on the experimental possibility of generating, with high accuracy and precision, arrays of spin color centers (for magnetic coupling) and connecting color centers with optical elements (for the long-range optical interaction). For example, a few approaches to the construction of an integrated platform for diamond photonics have been considered. The coupling of color centers to photons is crucial for building elements of quantum communication, such as quantum repeaters, and may improve readout accuracy for single-spin measurements. Technical requirements for the implementation of such entanglement schemes are similar to those for spin detection. Due to the combination of long spin coherence and strong optical transitions, color centers are promising candidates for the role of quantum communication elements.

One of the priority applications of single color centers is the development of magnetic field sensors for the detection, with nanometer spatial resolution, of superweak fields generated by single electron and nuclear spins. Such spin sensors based on strongly localized color centers can be placed in close proximity to external spins, at distances for which their respective magnetic fields are high enough for sufficiently accurate measurement.

High-sensitivity detection and nanometer spatial resolution measurements of electric, thermal, and magnetic fields are challenging problems having a great influence on modern science and technology. A scanning probe single-spin magnetometer is already available in which the nanocrystal with color centers is attached to the probe of an atomic force microscope (AFM) combined with a confocal optical microscope.

Coherent control of single spins in silicon carbide at room temperature was realized for a family of centers with $S = 3/2$ and $S = 1$ [100–102, 107–110]. Long spin coherence time was demonstrated under the ambient conditions. Numerous studies give evidence that SiC is a promising system for application in atomic-scale spintronic and quantum technologies.

Figure 11a presents an example of optical alignment of spin level populations in an SiC crystal. Color centers are usually labeled by their phononless lines: VI, V2, V3, V4. The results of investigations of these centers with the use of electron paramagnetic resonance, ODMR, and electron nuclear double resonance are reported in our previous reviews [109, 110]. Illustrations of optical alignment of spin level populations in a zero magnetic field (300 K) are presented in Fig. 11a, which also shows a real image of an AFM probe with a silicon carbide nanocrystal at the tip to be used in a scanning magnetometer. Figure 11b presents an example of the structure of the color center with $S = 3/2$ in an SiC crystal with the hyperfine structure determined by the interaction with ^{29}Si nuclei.

Since a single defect can be detected only at a low density of such defects, low-density electron irradiation

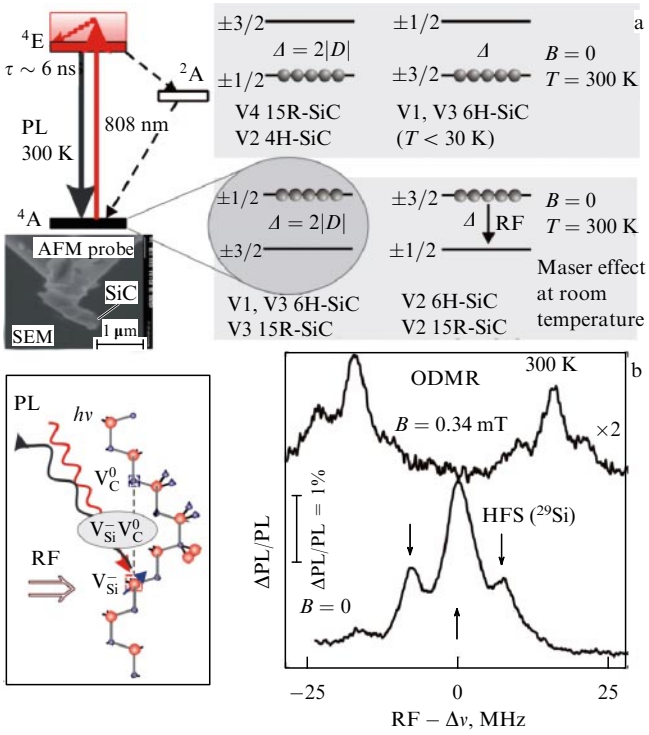

Figure 11. (Color online.) (a) Example of optical alignment of spin level populations in an SiC crystal. Color centers are usually labeled by their zero photon lines (ZPLs): V1, V2, V3, V4. The figure presents optical alignment schemes obtained at room temperature in a zero magnetic field; also shown is a real image of an AFM probe with an SiC nanocrystal at the tip to be used in a scanning magnetometer. SEM is the scanning electron microscope, $2|D|$ is the fine structure splitting in the zero magnetic field of axial symmetry, where D is the fine structure splitting parameter in the standard spin Hamiltonian. (b) Example of color center structure with $S = 3/2$ and typical ISFLS spectra of spin centers in an SiC crystal where the frequency of spin level splitting $\Delta\nu$ in a zero magnetic field is taken to be zero (see Fig. a). HFS is the hyperfine structure.

($10^{12} - 10^{13}$ cm^{-2}) with an energy of 2 meV was used. Such irradiation generates spin color centers uniformly distributed over the crystal at a concentration of $\sim 10^{11}$ cm^{-3} and a mean distance between defects of the order of 1 μm. Since the PL intensity of a single emitter is the main factor determining all subsequent applications, a special structure needs to be created, e.g., the use of metamaterials or microlenses can enhance photon collection efficiency. Pulsed methods, including electron spin echo, were employed to determine the lower coherence time threshold T_2, which proved to be 160 μs. In other words, the time T_2 is analogous to that observed in diamond and even smaller.

Quantum technologies based on coherent control of color center spins in diamond and silicon carbide have been developing rapidly in the past two decades. Combining ultrasensitive optical methods for the high-resolution detection of images and reliable coherent control with the use of nuclear magnetic resonance are key components in designing the first quantum devices based on these materials. The capability of high accuracy scaling of color centers and reaching long coherence times opens new prospects for so-called hybrid quantum processes in which color centers are associated with different types of qubits. There is little doubt that this research area will rapidly develop in the near future and can be expected to lead to the appearance of new quantum technologies. It is expected that applications based

on magnetometry and visualization techniques will be given additional impetus after the appearance of commercial devices based on diamonds and silicon carbide in the coming years.

5. Magnetization switching in ferromagnetic nanoheterostructures by electric pulses

It was mentioned in the Introduction that magnetoresistance-based spintronics is already finding wide application in memory devices. However, only 'passive' elements have thus far been realized; they allow reading out information but not processing it. The treatment of information implies the use of nonlinear elements, at least of the trigger type, and the possibility of controlling magnetization of selected elements. An obvious solution is to apply magnetic field pulses, which, however, requires focusing magnetic flux into a nanoscale region (see Section 6.3.3). At present, one of the most promising methods for the creation of active elements based on magnetic metal spintronics consists of magnetization control by electric pulses. It permits overcoming the nonlocality problem, because the lower limit on the size is set by the superparamagnetic limit for magnetic nanoelements. As to the operation speed, there are reports on obtaining electric field pulses with the duration less than 10 ps [111]. Sections 5.1–5.4 present a theoretical analysis of magnetization switching by electric pulses.

5.1 Switching by spin-polarized current

The best explored mechanism of electrically-mediated magnetization control is that in which spin-polarized current induced by a massive ferromagnet (polarizer) is passed through a second ferromagnet (analyzer) separated from the former by an interlayer of normal metal. Ref. [112] proposes the first self-consistent and most frequently cited theoretical model based on the spin-transfer torque (STT) concept. The model assumes that the injected spin-polarized carriers induce coherent precession of magnetization in the analyzer and cause either parallel or antiparallel (depending on current direction) orientation of magnetizations of the two ferromagnets. Evidently, such switching is possible in structures thinner than the spin relaxation length ($\sim$ 50 nm for copper).

The first experiments on this effect were described in Refs [113–115]. Their results were interpreted in terms of the STT theory. However, these and later studies revealed disagreement between experimental and theoretical results. Specifically, gradual deviation of magnetization was observed instead of the predicted switching, and a hysteresis behavior of the current was also found. Further theoretical studies aimed to refine the theory [116–125] were based on the same principal provisions as in [112].

All these studies used the semi-classical approach, in which the electron spin is described in quantum-mechanical terms and its transport is based on the classical law of conservation of angular momentum. Such an approach is, strictly speaking, invalid for systems of initially parallel or antiparallel configurations, because the starting phase of their evolution is controlled naturally by spin quantum fluctuations, i.e., magnons. Moreover, the STT approach [112] ignores strong nonequilibrium of the electron system in small-size contacts. The authors of [126] made a certain effort to take into account nonequilibrium of the system, but the semi-intuitive approach they used lacked strict quantum-mechanical substantiation. A consistent quantum-mechanical approach to the problem of interest was developed in Ref. [127]. Its details are discussed in the present section together with a comparison of the proposed theory and previous theoretical models.

Let us consider a system of two ferromagnetic layers: a polarizer with magnetization $\mathbf{M}_\mathrm{P}$ and analyzer with $\mathbf{M}_\mathrm{A}$ having a lateral size of 10 nm and a thickness of several nanometers separated by a normal metal interlayer of comparable thickness. Let us suppose that this structure sandwiched between two massive pieces of normal metal forms a nanocontact of a smaller size than the spin relaxation length ($\sim$ 50 nm). The passage of current in the vicinity of the polarizer induces a difference in chemical potential for spins directed differently with respect to the direction of $\mathbf{M}_\mathrm{P}$. The magnitude of the chemical potential difference depends on the difference between polarizer resistances ΔR_p for the spins of the two indicated directions and its sign depends on the sign of the applied voltage. If the contact size is assumed to be smaller than the energy relaxation length, the expression for the electron distribution function has the form

$$f_{\mathbf{k},\sigma} = \frac{1}{2}\left\{\left[1 - r\left(\frac{1}{2}+\sigma\right)\right] f_0\left(\epsilon_{\mathbf{k},\sigma} + \frac{eV}{2}\right) + \left[1 + r\left(\frac{1}{2}+\sigma\right)\right] f_0\left(\epsilon_{\mathbf{k},\sigma} - \frac{eV}{2}\right)\right\}. \quad (8)$$

Here, $r = \Delta R_\mathrm{p}/R$, where R is contact resistance disregarding the contribution of ferromagnetic layers, σ is the electron spin, and $\epsilon_{\mathbf{k},\sigma}$ is the electron energy. Below we use the kinetic equation for the magnon distribution function N_ω in the analyzer, taking account of magnon–electron interaction [127].

It can be shown that if due to spin polarization the chemical potential for electrons polarized along the analyzer magnetization direction exceeds the chemical potential of oppositely polarized electrons by the value greater than the magnon energy $\hbar\omega$, then the situation is unstable with respect to the avalanche-like increase in the magnon concentration. The corresponding condition can be expressed as $eVS_z/\hbar\omega < -1$, where $S_z = r(\mathbf{M}_\mathrm{A}\mathbf{M}_\mathrm{P}/(2M_\mathrm{A}M_\mathrm{P}))$ is the projection of analyzer magnetization onto polarizer magnetization with a weight determined by the degree of current polarization.

A rise in magnon concentration leads to a sharp increase in electron-magnon scattering efficiency in the analyzer with characteristic time $\tau_\mathrm{m-e}$, which suppresses spin flow polarization and disturbs the distribution (8). Note that magnon emission is naturally restricted by spin current density $j_\mathrm{s,inj}$. Therefore, transition from the voltage-controlled regime in which expression (8) is preserved to the current-controlled regime can be expected. To estimate the critical magnon concentration at which the transition occurs, the equation

$$\frac{\mathrm{d}n_\mathrm{m}}{\mathrm{d}t} = \left(\frac{\mathrm{d}n_\mathrm{m}}{\mathrm{d}t}\right)_\mathrm{emis} + \left(\frac{\mathrm{d}n_\mathrm{m}}{\mathrm{d}t}\right)_\mathrm{decay}, \quad (9)$$

obtained by integration of the initial kinetic equation over phase volume, is used. Here, n_m is the magnon concentration. The fulfilment of (8) yields

$$\left(\frac{\mathrm{d}n_\mathrm{m}}{\mathrm{d}t}\right)_\mathrm{decay} = -\frac{1}{\tau_\mathrm{m-e}}\, n_\mathrm{m}\,. \quad (10)$$

The emission term is limited by density $j_{s,inj}a^3/t_A$ of the spin-polarized current injected into the analyzer, where t_A is the analyzer thickness and a is the lattice constant.

For voltages close to the threshold value V_c (the respective critical value $j^c_{s,inj}$), the crossover between the two regimes occurs at

$$n_{m,c} = \tau_{m-e} j^c_{s,inj} \frac{a^3}{t_A} . \quad (11)$$

As shown in [127], $\tau_{m-e} = k_F t_A/\omega$, whereas $j_{s,inj} \sim \eta S_z e V v_F D(\epsilon_F)$, where $D(\epsilon_F) \sim a^{-3}\epsilon_F^{-1}$ and $\eta = j_{s,inj}/j^{ball}_{s,inj} \ll 1$. Hence, $n_{m,c} \sim \eta_c$. Here, $j^{ball}_{s,inj}$ is the spin-polarized current density that would be realized at the same voltage in the ballistic regime, D is the density of electronic states, and v_F is the Fermi velocity. Note that magnon absorption in the respective regime appears to be suppressed too, so that, without taking other factors into account, the increase in n_m cannot be limited up to $n_m \sim 1$.

Let us compare the presented theory with the previous approaches [112, 126] as well as [121–123]. In Ref. [112], spin transfer from the electron flow is proportional to the magnetization precession amplitude, so that the spin-polarized current does not generate a torque at $\mathbf{M}_P$ either parallel or antiparallel with respect to $\mathbf{M}_A$, in contrast to the approach being considered where spontaneous magnon emission occurs in these special cases too. In [112], the spin transfer from the electron flow is $j_{s,inj}\sin\zeta$ given that $t_A > l_p \sim (1/k_F)\epsilon_F/E_{ex}$. Here, E_{ex} is the exchange energy, l_p is the spin precession length, and ζ is the precession angle.

The evolution of precession angle ζ is described by Eqn (17) from Ref. [112] that takes the following form in our notations:

$$\frac{d\zeta}{dt} = -\left(\alpha\omega - \frac{j_{s,inj}a^3}{t_A}\right)\sin\zeta , \quad (12)$$

where α is the Gilbert damping parameter. For comparison with our results, it is necessary to take into consideration that the number of coherently excited magnons n_m is related to small ζ as $n_m \sim \zeta^2/2$. Then, the product $\alpha_0\omega$ is identified as magnon relaxation time $1/\tau_m$. As a result, Eqn (12) takes the form

$$\frac{dn_m}{dt} = \left(\frac{j_{s,inj}a^3}{t_A} - \frac{1}{\tau_m}\right)n_m . \quad (13)$$

For configurations close to collinear ones, Eqn (13) is analogous to that used in Ref. [123], designed to generalize Slonczewski's and Berger's ideas taking into account the electron mechanism of Gilbert damping [122].

Comparing (13) with our results leads to the following conclusions:

(1) Equation (13) shows that the STT approach corresponds in our terms to the current-controlled regime and does not describe the case of small ζ.

(2) Basing on the presented estimates one can show that the V_c switching threshold obtained in the framework of STT is identical to that obtained in our approach.

(3) The term responsible for the increase in the precession angle in (13) contains factor n_m, unlike the term describing magnon emission in (9). Because the condition $n_m \ll 1$ is fulfilled for small ζ, our approach predicts a faster evolution of analyzer magnetization.

(4) Our estimates show that the evolution of analyzer magnetization starting from the collinear situation can, in principle, proceed to the STT scenario at large n_m or, respectively, at large precession angles ζ.

(5) At high magnon pumping levels, i.e., in the case of violation of condition $n_m \ll 1$, the question arises as to the character of the subsequent evolution: whether it complies with the above noncoherent scenario or with the coherent one discussed in [112]. It can be expected that the inclusion of magnon–magnon processes in the consideration may lead to the achievement of coherence, by analogy with the prediction for acoustoelectric generators, in which phonon–phonon processes may cause conversion of amplified acoustic noise into a coherent sound wave [128].

Note also that magnon–magnon processes, the role of which was qualitatively analyzed in our work [128], allow the explanation of experimental findings that cannot be described in the framework of the STT approach, including system stabilization at finite precession angles.

5.2 Switching by an electric field controlling indirect exchange

One more potential mechanism underlying the influence of electrical effects on magnetization can manifest itself in ferromagnetic structures with indirect Ruderman–Kittel–Kasuya–Yosida exchange. In the simplest case, this structure is composed of two ferromagnetic layers separated by an interlayer of normal metal thin enough to make noticeable the efficiency of indirect exchange between the layers. An electric field applied to such a structure affects the electron system that mediates the indirect exchange. The possibility of such an effect was documented for the first time in Refs [129, 130] that report experiments with systems having a tunneling interlayer between ferromagnetic layers. Later authors (see [131, 132]) considered the influence of electrical effects on indirect exchange, but they experimented with massive systems in which it was difficult to ensure uniformity of exchange over the sample cross section. Moreover, some conclusions in these papers are contradictory.

We proposed in Ref. [133] a consistent theory of the influence of nonequilibrium caused by applied voltage on indirect exchange in structures placed in a normal metal point contact. The exchange interaction between two spins is known to have the form [134]

$$U^{int} = 2J^2\mathbf{S}_i\mathbf{S}_j\sum_{\mathbf{k},\mathbf{k}'}\frac{(f_{\mathbf{k}} - f_{\mathbf{k}'})\exp\left[i(\mathbf{k}-\mathbf{k}')\mathbf{R}_{ij}\right]}{\epsilon_{\mathbf{k}} - \epsilon_{\mathbf{k}'}} , \quad (14)$$

where J is the exchange energy, and R_{ij} is the vector connecting spins i and j. It can be shown that in the general case the interaction energy of the layers can be expressed as

$$U^{int}_{ij} = -2J^2\mathbf{S}_i\mathbf{S}_j\frac{a^3}{8\pi^3\epsilon_F k_F R^2_{ij}}\int_0^\infty dk\, k f_k \sin(2kR_{ij}) , \quad (15)$$

from which it is seen that the indirect exchange is due to Friedel oscillations of electron density. In the framework of our approach, we ignore the possibility of spin polarization of the current passing through the contact. In the case of a ballistic contact, the distribution function in its center has the form [135]

$$f_{\mathbf{k}} = \theta(k_x)F_0\left(\epsilon + \frac{eV}{2}\right) + \theta(-k_x)F_0\left(\epsilon - \frac{eV}{2}\right) , \quad (16)$$

where x is the contact axis, θ is the Heaviside function, and F_0 is the equilibrium distribution function. For the coupling

energy between ferromagnetic layers calculated per unit area we have [136],

$$\frac{U^{\rm int}}{A} = \frac{J^2 m S_1 S_2}{16\pi^2\hbar^2}\,\mathcal{K}(k_{\rm F}d)\,, \tag{17}$$

where d is the interlayer distance, A is the contact area, S_1 and S_2 are localized spin values in the layers. Integration yields for function $\mathcal{K}$ in (17)

$$\mathcal{K} \sim \frac{1}{z^2}\left(\mathcal{G}(T)\sin z - z\,\frac{eV}{2\epsilon_{\rm F}}\,\mathcal{G}\left(\frac{T}{2}\right)\mathfrak{R}_1(z)\right). \tag{18}$$

Here,

$$\mathcal{G}(T) = \frac{4\pi m T L}{k_{\rm F}\hbar^2}\sinh^{-1}\frac{4\pi L m T}{k_{\rm F}\hbar^2}\,,$$

and $\mathfrak{R}_1(z)$ is the rapidly oscillating function of the order of unity. According to the obtained results, the voltage applied to the contact can alter the mutual orientation of ferromagnetic layer magnetizations.

Let us compare our approach with that in Refs [129, 131]. To our opinion, their authors implicitly used the fact of spin polarization of the current passing through the system, and, therefore, their considerations are similar to those in [112], whereas in our work [133], the effect is completely due to indirect exchange.

5.3 Current-free switching by an electric field controlling indirect exchange under the conditions of Coulomb blockade

One of the important disadvantages of the described methods of electrical magnetization control is the necessity to pass rather high currents through the controlled system, which inevitably leads to energy dissipation. It is therefore critical to develop methods that allow either essential suppression, or elimination of the dissipation. Such an approach has recently been proposed in [137], where the influence of an electric field on indirect exchange in a system with the Coulomb blockade between ferromagnets F1 and F2 is used. F2 is a grain separated from the massive F1 layer by a tunnel contact I (Fig. 12a). The control is implemented by applying a potential to the grain trough a gate.

The possibility of the manifestation of indirect exchange in structures containing a tunnel contact was pointed out, e.g., in Refs [129, 130]. We use some considerations developed by their authors in our approach. Specifically, we are interested in the effect taking place in the nanoscale F1–I–NM–F2 hybrid structure presented in Fig. 12a. Tunnel coupling hybridizes states in the bulk and in the grain. In the first tunnel transparency approximation $A_{\rm T}$, the propagating $|\alpha; b\rangle$ mode in the bulk acquires an additional component $|\alpha; g\rangle$ propagating in the grain and vice versa. The boundary conditions at the tunneling barrier $|\alpha; b\rangle = A_{\rm T}|\alpha; g\rangle$. A similar line of reasoning holds for $|\alpha; b, j\rangle$ modes arising as modes $|\alpha, b\rangle$ are scattered by the spin localized at the jth node in the bulk (Fig. 12b). We also take into consideration that state $|\alpha, g\rangle$ can undergo back scattering into the grain at the ith node and thereby form the scattered state $|\alpha; g, i\rangle$ (Fig. 12c). In turn, it creates addition $|\alpha; g, i; b\rangle$ in the second order tunneling amplitude in the bulk layer.

As a result, the propagating initial mode takes the form

$$|\alpha\rangle = |\alpha; b\rangle + |\alpha; g\rangle + \sum_j \left(|\alpha; b, j\rangle + |\alpha; b, j; g\rangle\right) + \sum_i \left(|\alpha; g, i\rangle + |\alpha; g, i; b\rangle\right). \tag{19}$$

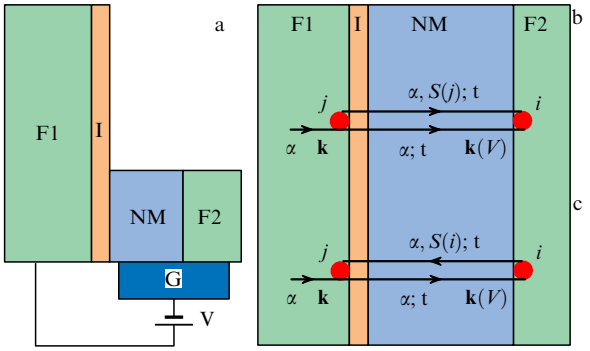

Figure 12. (Color online.) (a) Schematic of a structure with a tunnel junction for indirect exchange control: F1 is the FM polarizer, I is the tunneling barrier, NM is the normal metal, F2 is the FM grain, G is the gate. (b, c) Processes responsible for indirect exchange between j and i ions at the interfaces of FM layers F1 and F2, provided by the mode α with wave vector $\mathbf{k}$ from F1 layer. (b) Interference at the point of location of the ion i between the initial mode α; t, propagating through the tunnel junction and the layer of normal metal into the FM layer F2, and the mode $\alpha, S(j)$; t scattered at the ion j. (c) Interference at the point of location of ion j between the initial mode α and the mode $\alpha, S(i)$; t scattered at the ion i. Index t denotes the passed fraction of the wave localized in normal metal. Interferences modulate spin state density of delocalized α modes at the points i and j of ion locations. Modulation governs exchange interaction between F1 and F2. Dependence of $\mathbf{k}$ on the gate voltage V permits controlling the sign of the exchange integral.

A similar procedure is applicable to states β localized on the grain at $A_{\rm T} = 0$.

To recall, corrections for states α arising from hybridization with the grain are formed from β states having the same energy as the α mode. At the same time, electron tunneling from the bulk into the grain increases the Coulomb energy of the latter. If the valve generates potential V between the grain and the bulk, an electron with the kinetic energy ϵ in the bulk acquires, after tunneling into the grain, the kinetic energy $\epsilon' = \epsilon - eV - e^2/C$, where C is the grain capacity. If a hole tunnels, the state with energy ϵ in the grain binds to the state with energy $\epsilon' = \epsilon - eV + e^2/C$ in the bulk (Fig. 12b). Hole tunneling from the bulk into the grain corresponds to electron tunneling from the grain into the bulk and vice versa.

It should be noted that when taking into account tunneling processes involving α modes, the respective contributions describe electron tunneling into the grain, whereas the processes including β modes describe electron tunneling from the grain. At $|eV| < e^2/C$, real tunneling processes are suppressed by the Coulomb blockade and become virtual. However, the relationship between hybridized state energies persists, regardless of whether tunneling is real or virtual, because it does not depend on occupation numbers of the respective states. Virtual tunneling eliminates current through a structure.

In light of the foregoing, the expression for interaction energy takes the form

$$U^{\rm int}(\tilde{\mathbf{R}}) = J^2\mathbf{S}_i\mathbf{S}_j\,\frac{ma^3|A_{\rm T}|^2}{2\pi\hbar^2\tilde{R}}\sum_{\mathbf{k}',v}\Big\{2\exp\left[{\rm i}(\mathbf{k}'_v\tilde{\mathbf{R}} - k'_v\tilde{R})\right] + \exp\left[{\rm i}(-\mathbf{k}'_v\tilde{\mathbf{R}} - k'_v\tilde{R})\right] + \exp\left[{\rm i}(-\mathbf{k}'_v\tilde{\mathbf{R}} + k'_v\tilde{R})\right]\Big\}, \tag{20}$$

where $\mathbf{k}'$ corresponds to energy ϵ', $\tilde{\mathbf{R}}$ is the distance between the centers minus the thickness of the insulating layer, and $v = 1, 2$ corresponds to electron and hole channels. In the

subsequent summation, it should be taken into consideration that an electron can tunnel only from the filled state and a hole into the filled state. Accordingly, the upper bound of summation over k' in (20) is limited for $v = 1$ by the k_F value, whereas for $v = 2$ summation continues up to

$$k_h = k_F\left(1 + \frac{eV - e^2/C}{2\epsilon}\right).$$

We eventually arrive at expression (17) for the coupling energy between particles per unit area, in which S_1 and S_2 are the values of localized spins in the bulk and the grain, respectively. In the low voltage limit, the voltage-dependent part of $\mathcal{K}$ in (17) is estimated as

$$\mathcal{K}(z) \simeq -\frac{eV|A_T|^2}{2\varepsilon_F z}\cos\left[z\left(1 - \frac{e^2}{2C\varepsilon_F}\right)\right]. \quad (21)$$

The sign of the respective contribution to the exchange energy varies with the voltage sign. Note that the described effect, unlike the mechanisms proposed in [112, 129, 130], is realized in the absence of current through the device, which permits energy dissipation to be avoided.

5.4 Ultrafast magnetization switching in ferrimagnetic structures

A conceptually new approach to current-induced switching of magnetization can be implemented based on the recently discovered peculiarities of ultrafast spin dynamics in metallic ferrimagnetic alloys consisting of a rare-earth element and a transition metal (RE-TM) [138–140]. These and some other experiments have demonstrated ultrafast (a few picoseconds) magnetization switching of the amorphous metallic ferrimagnetic alloy GdFeCo under the impact of single femtosecond laser pulses. An important feature of such switching is its independence of pulse polarization [141], giving evidence that a laser pulse is not a source of angular momentum during switching but ensures rapid heating of the electron system (see also Section 6.2.1). Magnetization switching in such a strongly nonequilibrium system is a result of the nontrivial dynamic behavior of magnetic subsystems of a metallic ferrimagnet [140, 142]. Bearing in mind that the ultrafast magnetization switching in ferrimagnets is induced by the rapid heating of the electron subsystem, the authors of [143] proposed a theoretical model of such switching and suggested that short current pulses passed through a ferrimagnet-containing heterostructure can serve as an external stimulus triggering this process.

The model proposed in [143] takes into account the main characteristics of the equilibrium state of ferrimagnetic metals and their response to femtosecond optical excitation:

(1) a ferrimagnet structure consisting of two antiferromagnetically coupled ferromagnetic subsystems (A and B) is considered (Fig. 13a). The ferromagnetic properties of the subsystems are due to strongly localized f- and/or d-electrons; also, the structure contains an s(p)-electron subsystem strongly interacting with both ferromagnetic subsystems;

(2) it is supposed that more mobile s(p)-electrons control energy and angular momentum balance in the system. Specifically, they ensure spin relaxation with characteristic time τ_s via interaction with the lattice;

(3) demagnetization of ferromagnetic subsystems A and B by heating the electron subsystem is mediated through s(p)-electrons by virtue of spin exchange with the respective subsystems with characteristic times τ_{Ae} and τ_{Be} on the assumption that electron heating takes much less time than spin kinetic times (especially exchange scattering time).

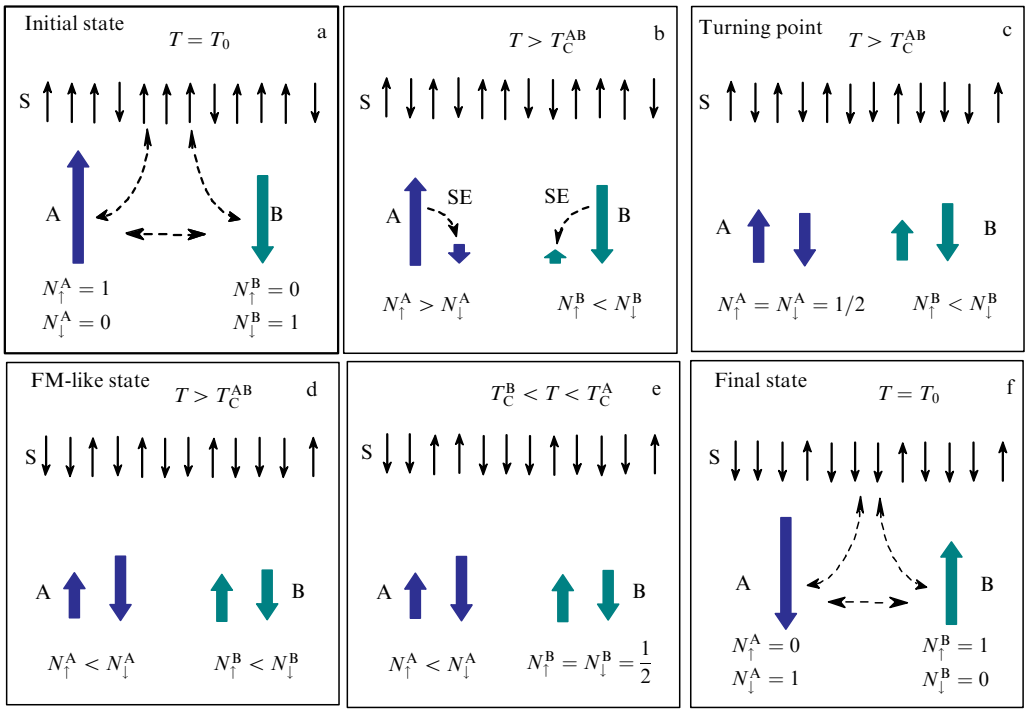

Figure 13. (Color online.) 'Snapshots' of the evolution of three electron subsystems of a ferrimagnetic metallic alloy. (a) Equilibrium system in which exchange interaction (dashed lines) between A (3d) and B (4f) subsystems occurs via s(p) conduction electrons. (b–e) Stages of magnetization evolution in A and B subsystems under a femtosecond rise in electron temperature T (see the text). SE is Stoner excitation resulting from electron spin flip in sublattices of a nonequilibrium system. (f) Final equilibrium state with switched magnetizations of both subsystems.

Gradual cooling of the electron subsystem results from energy transfer into the lattice by s(p)-electrons.

A conspicuous feature of this model is that the ferromagnetic system A characterized by stronger magnetization in equilibrium has a shorter demagnetization time ($\tau_{Ae} < \tau_{Be}$) (Fig. 13b). At a certain moment, subsystem A totally loses magnetization, whereas subsystem B partly retains it (Fig. 13c). It can be shown that spin conservation in the exchange electron–electron scattering enables s(p)-electrons to transport spin from B to A and thereby make the magnetization direction for subsystem A opposite to the initial one (Fig. 13d). Spin population dynamics in subsystems A and B, $N_{\uparrow\downarrow}^{A,B}$, at this moment designated as the 'turning point' t_r, can be described by the kinetic equation [143]

$$\left.\frac{dN_{\downarrow\uparrow}^{A}}{dt}\right|_0 \sim -\frac{(\tau_{Ae}\tau_{Be})^{-1}}{(4/\tau_s)+(1/\tau_{ee})}\left(N_{\uparrow\downarrow}^{B}-N_{\downarrow\uparrow}^{B}\right), \qquad (22)$$

where τ_{ee} is electron–electron scattering time in the s(p)-subsystem. If electron temperature in the vicinity of t_r drops to below the critical value T_C^A for subsystem A as a result of cooling, the system begins to restore its magnetization in the direction set by subsystem B. This gives rise to the ferromagnetic-like state observed experimentally in [142]. Meanwhile, demagnetization of subsystem B, for which $T_C^B < T_C^A$, continues (Fig. 13e); thereafter, its magnetization starts to be restored under the effect of exchange interaction with subsystem A.

It follows from the model proposed in [143] that the possibility of switching depends on the delicate balance between exchange electron–electron scattering times and energy/spin relaxation times. It is therefore important to determine the dependences of these times on ferrimagnetic alloy or heterostructure parameters. Our model confirms that the role of a laser optical pulse reduces to rapid heating of the sample, giving reason to suggest that switching can be effected by passing electric current through a properly prepared sample. In the future, it opens the way to ultrafast control of magnetization by electric pulses. The first report on the realization of such a possibility is Ref [144].

Reference [143] demonstrated theoretically that when passing a short current pulse through an A/NM/B ferrimagnetic heterostructure, where A and B are the layers of ferromagnetic metals and NM is the nonmagnetic metal interlayer, the complete demagnetization time of the subsystem A is $t_r \sim \tau_{Ae}E_{ex}^A/|eV - eV_c|$, and it can be controlled by applying voltages V in excess of the critical value $V_c = 2E_{ex}^A/e$.

Importantly, the total energy introduced into the system for an ultrashort switching time is low too since the heating of an electron system up to the critical temperature is concerned. It is expected that during the switching time the corresponding energy does not have time to transfer to the phonon system. It should be borne in mind that the thermal capacity of a phonon system in the respective temperature region is higher than that of an electron system. Therefore, the switching pulse does not cause local overheating of the lattice. Also, an important advantage of small double-layer devices ensues from the fact that each separate monolayer is a single-domain one due to its small size. This fact accounts inter alia for the sign of the anomalous Hall effect being completely determined by the magnetization sign. Therefore, the possibility of 'reading out' the status of a device appears that makes it a direct analog of an ordinary trigger.

6. Ultrafast optical control of anisotropy and dynamic phenomena in magnetic structures

A special branch of physics, femtomagnetism, dealing with interactions between femtosecond laser pulses and magnetically ordered media, emerged after the publication of Ref. [145] in 1996. The active development of this discipline is evidenced in numerous reviews of femtomagnetism [17], ultrafast optomagnetism [146], localization of nanometer-scale optomagnetic events [147], optical switching of magnetization in metals [148], picosecond magnetoacoustics [149], optospintronics [150], etc. In Sections 6.1–6.3, we will focus on one, but a wide class of femtomagnetic phenomena, namely laser-induced control of magnetic anisotropy, which, to our opinion, opens up promising prospects for the creation of spintronic devices.

6.1 Laser-induced changes of magnetic anisotropy and magnetization precession

Let us consider the phenomenological theory providing a basis for the classification of effects of ultrafast laser-induced change of magnetic anisotropy and the choice of approaches to their detection. For a thin infinite film, the contribution to the free energy responsible for equilibrium magnetic anisotropy has the form

$$F^{MA} = F^{MCA} + F^{g} + 0.5\mu_0 M_z^2,$$

where M_i is the projection of magnetization $\mathbf{M}$ onto the i-axis, and F^{MCA} is the contribution to energy from magnetocrystalline anisotropy. For certainty, the z-axis is directed normally to the film surface. The contribution $0.5\mu_0 M_z^2$ describes the shape anisotropy of the ferromagnetic film. The contribution F^g takes into account additional anisotropy that is usually of a growth and magnetostrictive nature.

The equilibrium orientation of magnetization is determined by the minimum of the sum of F^{MA} and Zeeman $-\mathbf{MH}_{ext}$ energies, where $\mathbf{H}_{ext}$ is the external magnetic field. It is convenient to introduce the total effective magnetic field $\mathbf{H}_{eff} = -\partial F^{MA}/\partial\mathbf{M} + \mathbf{H}_{ext}$ to describe the equilibrium position of magnetization (Fig. 14a). If a laser pulse alters one of the contributions to F^{MA} or gives rise to other contributions, both the position and the depth of the $F^{MA} - \mathbf{MH}_{ext}$ minimum change in the general case, together with the direction and magnitude of the effective field $\mathbf{H}'_{eff} = \mathbf{H}_{eff} + \delta\mathbf{H}_{eff}$ (Fig. 14a). The dynamic response of magnetization to such changes is described by the nonlinear Landau–Lifshitz–Gilbert (LLG) equation. The solution of this LLG equation is the damped precession of magnetization. The $\delta\mathbf{H}_{eff}$-induced precession has a number of important features that distinguish it from precession induced by an alternating magnetic field. In the general case, the z'-axis of magnetization precessional motion (Fig. 14a) and precession frequency $\omega(t)$ are time functions; $z'(t)$ reflects the instantaneous direction of the total effective field $\mathbf{H}'_{eff}$ whose evolution in time is determined by relaxation processes responsible for variations in anisotropy after the laser-induced excitation. The precession frequency $\omega(t) = \gamma H'_{eff}(t)$ is likewise related to $\mathbf{H}'_{eff}$ evolution. The initial direction of magnetization motion setting the initial phase of precession is unambiguously related to the torque $\mathbf{T}_0$ at the starting moment of precession (Fig. 14a):

$$\mathbf{T}_0 = -\gamma\left(\mathbf{M}(t<0)\times\delta\mathbf{H}_{eff}\right). \qquad (23)$$

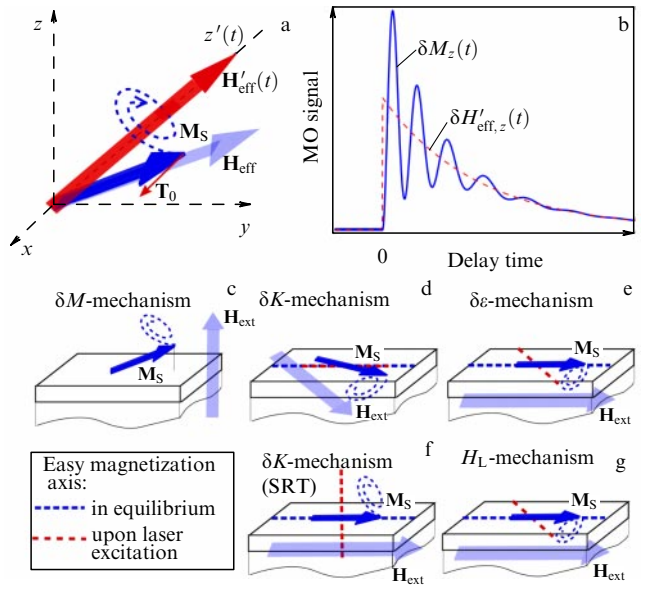

Figure 14. (Color online.) (a) Magnetization precession excited by a laser-induced change of magnetic anisotropy. (b) Example of magneto-optical response observed in this process. (c–g) Schematic representation of laser-induced change of anisotropy axes and magnetization trajectory.

Ultrafast laser-induced change of anisotropy can allow addressing several important problems. One of them is excitation of high-amplitude magnetization precession for switching from one equilibrium state to another. To achieve this goal, the character of evolution of $\mathbf{H}'_{\text{eff}}(t)$ and precession damping τ_0 must also meet the requirements for precessional switching [151]. An interesting problem in the context of this task is the excitation of nonlinear magnetic dynamics, which cannot be described by solving the linearized LLG equation. One more problem is tuning the precession frequency $\omega(t)$ and, in a more general case, control of the magnon dispersion relation to be applied in optically tunable magnon spintronics [152]. An interesting problem of excitation of high-frequency precession of magnetization for terahertz spintronics necessitates addressing these problems.

Magnetization precession is not only a result but also a 'probe' of laser-induced changes of anisotropy. The most detailed information about parameters of magnetization precession can be obtained by combining femtosecond pump-probe technique and vector magneto-optical magnetometry [153–156]. In most cases, however, laser-induced precession is detected by measuring the magneto-optical effect alone in one experimental geometry. Experiments considered in Sections 6.2, 6.3 are based on the detection of the polar magneto-optical (MO) Kerr effect or Faraday effects with temporal resolution and measuring the rotation angle of the polarization plane $\theta(t) \sim M_z(t)$ of probe pulses,

$$\theta(t) = A(t) + \theta_0 \exp\left(-\frac{t}{\tau_0}\right) \sin\left(\omega(t)t + \phi_0\right),$$

where the initial phase ϕ_0 is determined by the direction of $\mathbf{T}_0$ (23):

$$\phi_0 = \angle(\mathbf{T}_0, \mathbf{z}). \qquad (24)$$

The character of the $A(t)$ and $\omega(t)$ evolution is related to the evolution of the $\mathbf{H}'_{\text{eff}}$ direction and value as shown in Figs 14a, b illustrating the effect of a laser pulse resulting in a sharp change in $\delta\mathbf{H}_{\text{eff}}$ followed by slower exponential relaxation of $\mathbf{H}'_{\text{eff}}$ to the equilibrium direction and value of $\mathbf{H}_{\text{eff}}$.

6.2 Mechanisms of magnetic anisotropy changes

The processes leading to alteration of magnetic anisotropy and excitation of precession are conveniently categorized into several types as follows:

- change of magnetization magnitude (δM-process);
- change of anisotropy parameters (δK-process);
- appearance of additional anisotropy as a result of laser-induced dynamic strain ($\delta\varepsilon$-process);
- appearance of additional anisotropy axis as a result of electronic structure perturbation ($\mathbf{H}_{\text{L}}$-process).

The first two mechanisms are usually of a *thermal* nature, i.e., they result from the elevation of effective temperature of one of the medium subsystems (electrons, lattice). However, certain authors report a *nonthermal* character of δM- and δK-processes, largely in diluted magnetic semiconductors; the $\delta\varepsilon$-process can be just as well regarded as a nonthermal one even if it plays an important role in thermal processes. Clearly, $\mathbf{H}_{\text{L}}$-processes based on the population of selected excited electronic levels are nonthermal ones; their important feature is susceptibility to laser pulse polarization and low accompanying dissipation of energy.

6.2.1 Variation in shape anisotropy (δM-process). A pioneering study on laser-induced excitation of precession and spin waves is reported in Ref. [157], where thin Ni and permalloy films were excited by 100-fs laser pulses. An important feature of this experiment was the external magnetic field with a nonzero projection onto the film normal (Fig. 14c). In the equilibrium state, magnetization of the film with 'easy plane' anisotropy related to shape anisotropy $\mu_0 M_z^2$ was directed at a certain angle to the film surface and the $\mu_0 M_z^2$ contribution to F^{MA} had a nonzero value. This and numerous subsequent experiments with various magnetic metals showed that in such a geometry the magnetization response to femtosecond laser pulses contains two contributions.

At times of ~ 100 fs, ultrafast demagnetization occurs, i.e., a reduction in magnetization M_S takes place [145]. This process in itself makes one of the main contributions to femtomagnetism in metals (see [17, 148, 158–160]). The question of the microscopic mechanism behind ultrafast demagnetization remains open, even though it is understood that such a strongly nonequilibrium process relies on by absorption of laser pulse energy leading to a rise in electron effective temperature up to $T_{\text{e}} \sim 1000$ K or higher during ~ 10 fs. Thermalization with the lattice cools the electron subsystem and heats the lattice (T_{l}) by several hundred kelvin over several picoseconds [161]. The response of a spin system to such rapid considerable change in T_{e} and T_{l} is responsible for ultrafast demagnetization.

A decrease in the $\mu_0 M_z^2$ contribution to the free energy F^{MA} due to ultrafast demagnetization generates torque $\mathbf{T}_0 \perp z$ (23) sufficient to cause precession, since M_S changes during the time ~ 100 fs, i.e., a much shorter time than the characteristic magnetization precession period $2\pi/\omega \sim 100$ ps.

6.2.2 Variation of magnetocrystalline anisotropy (δK-process). In the general case, the condition for excitation of magnetization precession due to the δK-process, i.e., a laser-induced

change in anisotropy constants, is a nonzero angle between magnetization and the external magnetic field vector in the equilibrium state. In this case, a reduction in anisotropy constants leads to the deviation of the effective field $\delta\mathbf{H}'_{\text{eff}}$ necessary to induce precession (Fig. 14d). The action of laser pulses on a magnetic metal causes a picosecond rise in lattice temperature T_l, which suggests the possibility of a pronounced change of anisotropy parameters of a metal.

Note that the magnetic anisotropy energy in the range of temperatures significantly lower than the Curie temperature is characterized by a stronger temperature dependence than magnetization [162]. As early as in Ref. [157], the δK-process was already considered along with the δM-process.

A detailed study on ultrafast anisotropy variation in a thin Fe/MgO film by time-resolved vector magneto-optical magnetometry was reported in Refs [154, 155].The film plane had two perpendicular axes of cubic anisotropy. The external magnetic field was oriented in the film plane at an angle to these two axes to exclude excitation of precession due to shape anisotropy variation (δM-process). Excitation of the Fe film by femtosecond laser pulses caused magnetization precession that could be described in the model taking account of laser-induced heating of the lattice and the corresponding decrease in the cubic anisotropy constant [154, 155].

The vector magneto-optical technique with temporal resolution made it possible to completely reconstruct the spatial and temporal trajectory of magnetization movement and to determine how the direction of the total effective magnetic field varies in space and time. Based on these data, the authors of [154] deduced the magnitude of absolute laser-induced changes to the effective field of magnetocrystalline anisotropy, $\delta\mathbf{H}'_{\text{eff}} \sim -50\%$, and estimated respective lattice temperature rise $\Delta T_l \sim 350$ K.

Thin homogeneous and granulated films of magnetic metals with marked 'easy axis' anisotropy are of significance for spintronics. To excite precession in such films due to δK- and δM-processes, an external magnetic field $\mathbf{H}_{\text{ext}}$ needs to be applied at a certain angle to the film normal. Ref. [163] demonstrated excitation of magnetization precession in a granular $L1_0$-FePt/MgO film. Due to the strong spin-orbit interaction in this material, the effective field of uniaxial magnetocrystalline anisotropy amounts to $H_z^{\text{MCA}} \sim 10$ T. Strong anisotropy allowed exciting precession with a frequency of up to 400 GHz in the external magnetic field up to 7 T.

Laser-induced heating in magnetic dielectrics is much weaker than in metals, while the energy and angular momentum transfer channel responsible for ultrafast demagnetization in metals is inefficient due to the absence of free carriers. The characteristic time of laser-induced demagnetization in dielectrics is several hundred picoseconds [164, 165], which permits the δM-process to be ruled out as an excitation mechanism behind magnetization precession. Absorption of laser pulses with energies below the band gap is largely due to weak localized electron transitions, accounting for significantly weaker heating of the lattice ($\Delta T_l \sim 1-10$ K) than in metals. To what extent the δK-process is essential for the excitation of magnetization precession in dielectrics has for a long time remained an open question.

The authors of [165] investigated the response of a thin magnetic dielectric film of substituted yttrium iron garnet (S-YIG) to excitation by femtosecond laser pulses with a photon energy from 1.6 to 2 eV, corresponding to the relative transparency band (absorption ~ 100 cm^{-1}). They

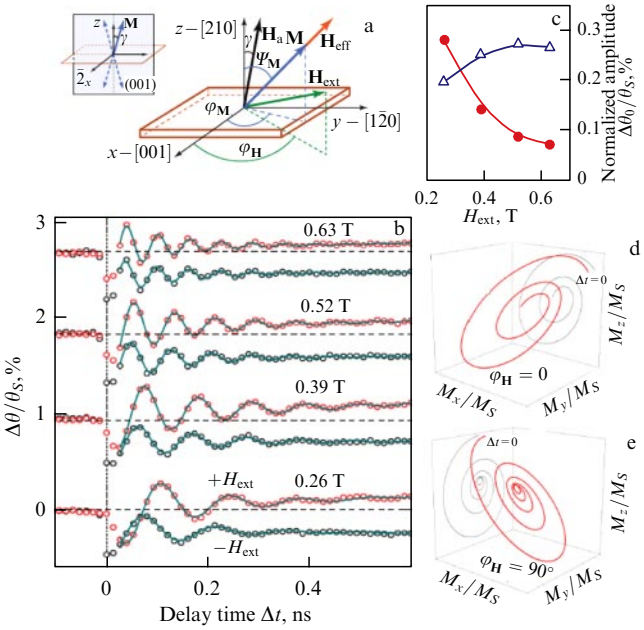

Figure 15. (Color online.) Magnetization precession in a S-YIG(210) film induced by the δK-process and ultrafast inverse Faraday effect [165]. (a) Total effective anisotropy field $\mathbf{H}_a$, equilibrium magnetization in the film and orientation of external magnetic field $\mathbf{H}_{\text{ext}}$. (b) Time dependences of laser-induced Faraday effect in the S-YIG film (210) at different values of external magnetic field $\mathbf{H}_{\text{ext}} \parallel x$ for probe pulses propagating along the z-axis. $\Delta\theta/\theta_s$ is the rotation of the probe pulse polarization plane. (c) Field dependences of normalized precession amplitude $\Delta\theta_0/\theta_S \sim \Delta M_z/M_S$ induced by δK-process (circles) and inverse Faraday effect (triangles). (d, e) Calculated precession trajectories of magnetization induced by δK-process in a field applied along the hard x-axis (d) and y-axis (e).

experimented with a sample of a $(YBiPrLu)_3(FeGa)_5O_{12}$ film grown by liquid-phase epitaxy on a $Gd_3Ga_5O_{12}$ substrate (gadolinium-gallium garnet, GGG) with orientation (210) (Fig. 15a). The growth anisotropy of such a film prevailed over the intrinsic cubic one and had uniaxial (K_u, K_i) and orthorhombic (K_{yz}) contributions $F^{\text{MA}} = K_u m_z^2 + K_i m_y^2 + K_{yz} m_y m_z$, where $m_i = M_i/M_S$ is the normalized projection of magnetization onto the i-axis (see Fig. 15). It can be shown [165] that the direction of torque $\mathbf{T}_0$ (23) in the δK-process associated with one or several anisotropy constants K_u, K_i, K_{yz} is given by the relationship between δK_u, δK_i, and δK_{yz}, on the one hand, and by the initial direction of magnetization $\mathbf{M}$ with respect to the axes determining growth-induced magnetic anisotropy, on the other hand. In the low-symmetric (210) S-YIG film, a rotation of the external field in the film plane changes the equilibrium direction of magnetization in a complicated manner, including alteration of all three projections of M_i. Determining the parameters of laser-induced magnetization precession for different values and directions of the external field allows evaluating the contribution of the δK-process to the excitation of magnetization precession.

The results of the experiment are presented in Fig. 15b. The initial precession phase ϕ_0 (24) at small values of field H_{ext} depends in a complicated way on the sign of the external magnetic field; the dependence becomes less apparent as the field increases. An analysis of the presented field dependence and the dependence on the polarization of exciting pulses [165] demonstrated that excitation of precession in large fields is due to the ultrafast inverse Faraday effect [146, 166]; in low

fields, an important contribution to excitation comes exactly from the laser-induced thermal variation of growth anisotropy constants.

Indeed, the direction of the total effective field in small fields H_{ext} differs from that of the external magnetic field and is largely dependent on anisotropy constants. The contribution from laser-induced variation in anisotropy becomes less essential as the external magnetic field increases (Fig. 15c). In other words, a maximum change in the total effective field $\delta\mathbf{H}_{\text{eff}}$ associated with the δK-process occurs in small external fields. Analysis of the dependence of the initial precession phase on the direction of the external magnetic field in the film plane showed that the initial phase of precession ϕ_0 (24) depends on this direction. Figures 15d, e present the results of the calculation of magnetization precession trajectories based on experimental data on δK_u, δK_i, δK_{yz}, and ϕ_0 for two orientations of the external magnetic field.

The authors of [167] excited magnetization precession in (Ga,Mn)As by the δK-process. The complicated precession trajectory revealed in the study enabled the authors to conclude that an essential contribution to precession excitation by the δK-process is due to the nonthermal alteration of balance between cubic (K_1) and uniaxial (K_u) contributions to anisotropy. The authors ascribed this alteration to appearance and relaxation of photoinduced holes [168]. Note that the excitation of precession in DFS (Ga,Mn)As also observed in [169] was attributed to the thermal δK-mechanism without a detailed analysis of the validity of this assumption.

6.2.3 Spin reorientation transitions (δK-process). A dynamic change in anisotropy constants in S-YIG (δK-process) was only a fraction of a percent, and the deviation of magnetization from equilibrium did not exceed 1° [165]. For greater magnetization deflections from equilibrium in dielectrics due to the δK-process, materials are needed in which relatively weak laser-induced heating would markedly change K. The most promising materials of this sort are dielectrics with *spin reorientation* (SR) transitions in a narrow range of temperatures [170], such as rare-earth orthoferrites $R\text{FeO}_3$. The rare-earth element R determines the presence, type, and temperature of the SR transition. In the general case, magnetic anisotropy of orthoferrites is expressed as $F^{\text{MCA}} = K_{u1}(T)\sin^2\zeta + K_{u4}\sin^4\zeta$, where ζ is the angle in the ac plane between the crystallographic a-axis of the orthorhombic crystal and magnetization. Constant $K_{u1}(T)$ for certain rare-earth orthoferrites changes sign depending on temperature. The sign of constant K_{u4} determines the type of SR transition associated with a change of the $K_{u1}(T)$ sign [170].

SR transition in orthoferrites is a result of the different temperature dependence of two competing contributions to $K_{u1}(T)$ [170]. The single-ion contribution from the spin-orbit interaction for Fe^{3+} ions is supplemented by the contribution coming from the interaction of Fe^{3+} magnetic moments with disordered R^{3+} magnetic moments. Rare-earth ions exhibit a strong temperature dependence of both magnetic moment and single-ion anisotropy. The contribution from single Fe^{3+} ion anisotropy stabilizing the weak ferromagnet phase ($\mathbf{M} \parallel c$ and $\mathbf{L} \parallel a$) predominates for all orthoferrites at temperatures below the Neél temperature (~ 650 K). The second contribution to anisotropy increases as temperature decreases, and two second-order SR transitions to the phase with $\mathbf{M} \parallel a$ and $\mathbf{L} \parallel c$ or first-order SR transition to the antiferromagnetic phase ($\mathbf{L} \parallel b$) occur at a certain temperature.

It was shown in a series of publications [171–174] that excitation of orthoferrite in the low-temperature phase by femtosecond laser pulses leads to excitation of magnetization precession as a result of a change of the $K_{u1}(T)$ sign during several picoseconds. The thermal nature of such an ultrafast SR transition is confirmed by the fact that the closer the initial temperature of the sample to the SR transition temperature the greater the laser-induced deflections of **M** and **L** from the equilibrium direction in the low-temperature phase [171–173]. The key intermediate process responsible for the change of sign of the anisotropy constant and the occurrence of the laser-induced SR transition is the variation in the populations of the rare-earth R^{3+} ion 4f-sublevels with increasing temperature. The characteristic time of this process is a few picoseconds; it determines the rate of the ultrafast SR transition [173].

It should be emphasized that the laser-induced SR transition exemplifies the δK process at which both the value and the sign of the anisotropy constant vary. It allows magnetization precession to be excited in an external magnetic field applied along the easy anisotropy axis in the low-temperature phase and even in the absence of a magnetic field. In the limiting case, the laser-induced SR transition consists of 90° rotation of the anisotropy axis, which makes possible the ultrafast switching of magnetization via the SR transition in the absence of an external magnetic field (see Section 6.3.1).

6.2.4 Inverse magnetostriction ($\delta\varepsilon$-process). It was shown in [175] that picosecond strain pulses ε_{ij} or packets of subterahertz acoustic phonons [176] injected into a ferromagnetic semiconductor (Ga,Mn)As film induce magnetization precession owing to inverse magnetostriction, i.e., as a result of an additional magnetoelastic contribution to magnetic anisotropy $F^{MS} = b\delta\varepsilon_{ij}m_i m_j$, where b is the magnetoelastic coefficient (see also Section 2.3). This finding laid the foundation of picosecond magnetoacoustics as a separate branch of femtomagnetism. The phenomenon of inverse magnetostriction forms the basis of the excitation of not only magnetization precession in DFS [175], metals [177], and dielectrics [178] but also exchange spin waves [69], forced large-amplitude oscillations of magnetization [179], and magnetoelastic waves [180].

It was demonstrated in [181] that, in a thin ferromagnetic metal film, the $\delta\varepsilon$-process may compete with the δK-process and thereby lead to the nontrivial dynamic behavior of magnetization. Indeed, the laser-induced heating of the lattice in a metal during a few picoseconds may be accompanied by thermal stress leading to dynamic strain ε_{ij} with a temporal and spatial profile resembling the temperature profile [176]. The authors of [181] experimented with a 100-nm-thick epitaxial film of the magnetostrictive metal galphenol (Fe,Ga) on a GaAs substrate (311). The external magnetic field was directed along the hard anisotropy axis in the film plane, which made possible the observation of magnetization precession triggered by a laser pulse via the δK-process and excluded the δM-process.

The experiment showed that the initial phase of precession ϕ_0 depends in a nontrivial manner on the magnitude of the external magnetic field and changed from 0 to 90° in the H_{ext} range between 150 and 500 mT (Fig. 16), which cannot be explained by the effect of the δK-process. Such a dependence of ϕ_0 reflects the complicated variation of torque direction $\mathbf{T}_0$ (23) and competition between two mechanisms underlying

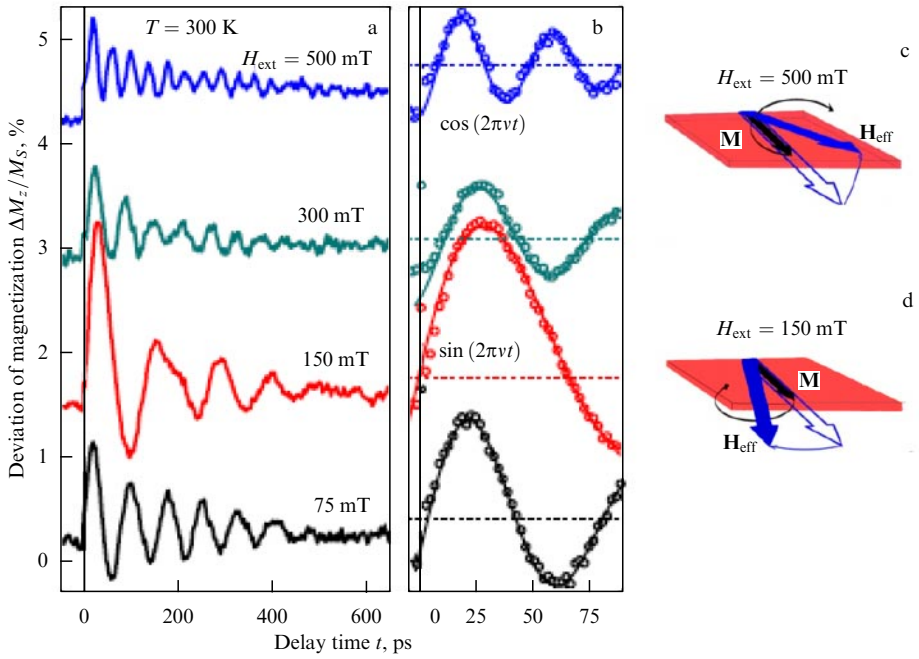

Figure 16. (Color online.) Magnetization precession in a (Fe, Ga)/GaAs(311) film induced by δK- and $\delta\varepsilon$-processes [181]. (a, b) Time dependences of the laser-induced polar MO Kerr effect in the (Fe, Ga)/GaAs(311) film at different values of magnetic field $\mathbf{H}_{\text{ext}}$ applied along the hard axis in the film plane shown at various time scales. (c, d) Illustrations of the trajectory of laser-induced change in the total effective field and magnetization precession trajectory at field values of 500 and 150 mT.

excitation of magnetization precession. One of them, the δK-process, is largely responsible for the rotation of the effective field in the film plane, i.e., $\mathbf{T}_0 \| z$ and $\phi_0 = 0$. A rise in lattice temperature also leads to quasi-stationary longitudinal and shear strain, the latter being due to the low symmetry of the (Fe,Ga)/GaAs(311) film.

Importantly, the shear strain gives rise to an additional anisotropy axis directed normally to the film surface, which results in a contribution to the torque $\mathbf{T}_0 \perp z$, and the initial phase ϕ_0 of the signal becomes nonzero. Experiment [181] revealed a significant difference between δK- and $\delta\varepsilon$-processes. The contribution of the δK-process to the generation of magnetization precession in the selected geometry prevails in weak magnetic fields, whereas the $\delta\varepsilon$-process effectively excites precession in strong fields too when equilibrium magnetization is aligned with the external magnetic field, making it possible to use the $\delta\varepsilon$-process to excite high-frequency magnetization precession.

To recall, laser-induced strain in metals may result not only from rapid lattice heating but also from ultrafast demagnetization; the contribution of the latter to the $\delta\varepsilon$-process can be different from that expected based on classical concepts of magnetostriction [182]. The role of such strains in the excitation of magnetization precession remains to be elucidated. Moreover, the mechanism of strain emerging under optical excitation may be different from the thermal one; e.g., it can involve deformation potential in semiconductors [183] and therefore be of importance for the optical excitation of magnetization dynamics in magnetic semiconductors.

6.2.5 Ultrafast photomagnetic phenomena ($\mathbf{H}_L$-process). An alternative approach to controlling magnetic anisotropy is based on a special class of *photomagnetic* phenomena [184] related to photoinduced anisotropy. For example, in ferrite garnets with some of the Fe^{3+} ions substituted by Co^{2+} ions (Co:YIG), the polarization-dependent photo-induced charge transfer between Co^{2+} and Fe^{3+} or repopulation of Co^{2+} excited states results in an additional anisotropy axis [185]. The excitation of magnetization precession by virtue of the ultrafast photomagnetic effect in a S-YIG/GGG film was observed for the first time in [186] with a $\sim 1^\circ$ magnetization deviation from equilibrium. Ref. [187] reported an analogous fast photomagnetic effect induced by a surface electromagnetic wave in a S-YIG/GGG film with a plasmonic structure created on the surface. Such an approach can be used in the future for the enhancement of the ultrafast photomagnetic effect and other laser-induced phenomena [147].

An important step in obtaining large angles of deviation of the effective field and magnetization from equilibrium values is the excitation of Co:YIG films by linearly polarized fs laser pulses. It was shown in [188] that linearly polarized pulses excite precession with a $\sim 20^\circ$ amplitude deviation from equilibrium and the initial phase set by pulse polarization. Figure 17a presents time dependences of the Faraday effect (FE) in a Co:YIG film at two values of the external magnetic field H_{ext}. An important result of the experiment is that the magnetization precession frequency $\omega(t)$ depends on time, and the laser-induced effective field $\delta\mathbf{H}_{\text{eff}}$ has a characteristic lifetime of ~ 20 ps (Fig. 14b).The magnetization precession amplitude depends on the orientation of the laser pulse electric field vector with respect to crystal axes (Fig. 17b), which indicates precession excitation due to the ultrafast photomagnetic effect rather than the δK-process. Later studies demonstrated the important role of photon energy of the exciting pulse in this process [189].

6.3 Ultrafast anisotropy changes and spintronic phenomena

6.3.1 Optical switching of magnetization. Optical switching of magnetization appears to be the Holy Grail of femto-

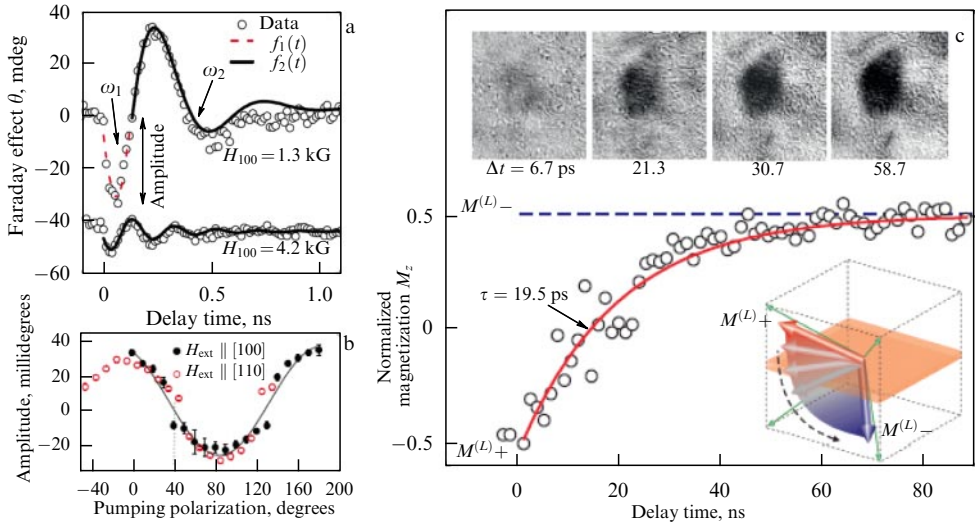

Figure 17. (Color online.) Laser-induced magnetization precession [188] and switching [190] in Co:YIG film due to the $\mathbf{H}_L$-process (a) Time dependences of the Faraday effect (FE) in Co:YIG in the case of excitation by linearly polarized laser pulses [188]. (b) Dependence of FE oscillation amplitude on laser pulse polarization measured for two directions of an external magnetic field. (c) Evolution of magnetization M_z projection in Co:YIG for magnetization switching induced by a single linearly polarized laser pulse [190]. The inset shows single-pulse magnetooptical images at various delay times.

magnetism, which accounts for the exceptional attention to this phenomenon in ferrimagnetic metals (see the discussion in Section 5.4). In the present section we discuss two alternative methods for switching magnetization based on the effect of a laser-induced change in anisotropy in magnetic dielectrics.

Precessional switching of magnetization in Co:YIG. The significant dynamic deviation of magnetization reached in the experiments on Co:YIG [188] described above made it possible to use this material for optically-induced precessional switching of magnetization [189, 190]. Using the technique of time-resolved single-pulse magnetooptical microscopy [139], the authors of [190] employed this method to evaluate the final and intermediate states of Co:YIG film after its exposure to linearly polarized laser pulses. Measurements were made in a zero external magnetic field. One of the main results of the experiment is presented in Fig. 17c, showing the formation of a domain with magnetization directed at an angle of 90° to the initial one induced by a linearly polarized laser pulse. The authors of [190] demonstrated, based on polarization and intensity dependences of the laser-induced evolution of magnetization, that the switching between two magnetization directions is precessional and occurs due to the ultrafast photomagnetic effect considered in Section 6.2.5. Important factors that provide the switching were not only the value and direction of the laser-induced anisotropy field but also its relatively short lifetime (20 ps), preventing the precessional return of magnetization to the initial state.

An important feature of such Co:YIG magnetization switching [190] is spectral selectivity [189] apart from record-breaking low heat dissipation [190]. It was shown that tuning the central photon energy of a laser pulse makes possible the selective excitation of transitions in 3d-shells of Co^{2+} ions occupying tetrahedral or octahedral positions in a Co:YIG film and thereby alteration of the polarization dependence of the ultrafast photomagnetic effect.

Switching magnetization via SR transition in orthoferrites. Ultrafast magnetization control based on laser-induced transitions in orthoferrites was implemented in a series of publications [191–194]. Ref. [192] reports a second-order SR transition in $(Pr, Sm)FeO_3$ induced by individual circularly polarized pulses in a zero magnetic field and shows that the high-temperature phase domain forms already at times of the order of 5 ps with the direction of magnetization **M** determined by a combination of three factors, namely, energy density in the exciting pulse, its polarization, and initial sample temperature. It is shown that this unique switching scenario is due to the fact that the magnetic dynamics is triggered by the δK-process together with the ultrafast inverse Faraday effect. The ultrafast second-order SR transition was used in [193] to control Co film magnetization in the $Co/SmFeO_3$ structure.

A specific feature of the laser-induced first-order SR transition is that it is accompanied by the development of net magnetization [191, 194]. It was shown in [194] that the action of single linearly polarized laser pulses on $DyFeO_3$ in the low-temperature phase (Fig. 18a) actually results in emerging of a domain with nonzero magnetization. The orientation of this magnetization depends on laser pulse polarization and the initial orientation of the $\pm\mathbf{L}$ vector (Fig. 18b). To recall, 180°-antiferromagnetic domains $L\pm$ are indistinguishable in many experiments. The authors of [194] showed that the laser-induced transition is accompanied by precession at the soft mode frequency (Fig. 18c), with the initial phase given by the ultrafast inverse Cotton–Mouton effect [195].

Importantly, rare-earth orthoferrites constitute only one of the groups of materials exhibiting SR transitions. There are a number of dielectrics, including those such as hematite α-Fe_2O_3 and magnetite Fe_3O_4 undergoing SR transitions, the mechanism of which differs from that described in the preceding paragraphs. Realization of an ultrafast SR transition in these and other materials may give rise to new approaches to magnetization control.

Worthy of mention is the fundamental difference between photomagnetic switching in Co:YIG and that via the SR transition in orthoferrites. In the former case, sequential switching between different states can be realized, and magnetization in the new state persists infinitely long. In the

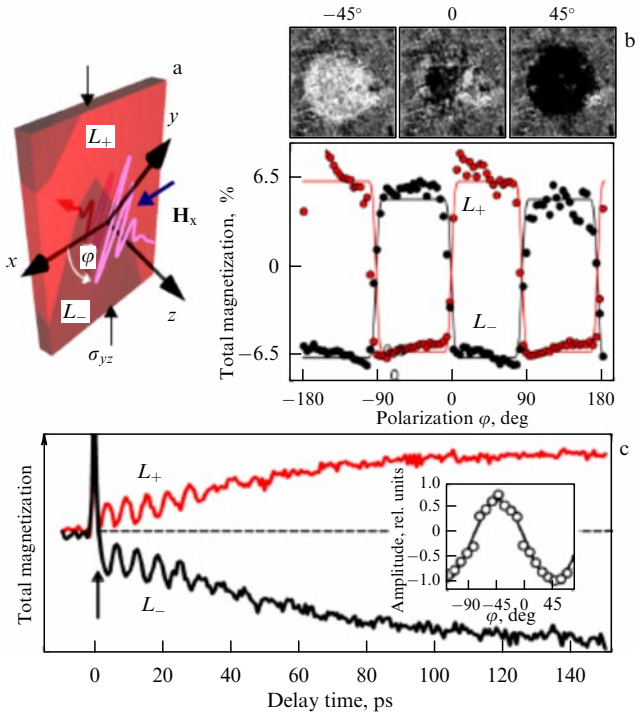

Figure 18. (Color online.) Emergence of net magnetization in $DyFeO_3$ due to SR transition induced by linearly polarized laser pulses [194]. (a) Geometry of experiment. (b) Net magnetization induced in $L\pm$ domains upon excitation by linearly polarized pulses and its dependence on polarization. The inset shows single-pulse images. (c) Temporal evolution of bulk magnetization induced in $L\pm$-domains upon excitation by linearly polarized laser pulses and polarization dependence of precession amplitude (inset).

latter case, switching occurs from the low-temperature phase to the high-temperature one, and the laser-induced phase relaxes to the initial state at times of about 1 ms, depending on sample cooling. However, it was proposed in [196] to realize a laser-induced effective upward shift by 1 K of the SR transition temperature in $DyFeO_3$; in the long run, this can facilitate realization of an ultrafast SR transition from the high-temperature to the low-temperature phase.

6.3.2 Optically induced spin transport. Issues important for the further development of spintronics include the generation and transfer of angular momentum in the form of spin-polarized current and spin waves or magnons. In this section, we consider how a laser-induced change in anisotropy can initiate spin pumping and related phenomena. One more topical problem is the optical generation of magnetostatic waves and controlling their parameters. At present, the main mechanism for optical generation of magnetostatic waves is the ultrafast inverse Faraday effect [197], but Refs [198–200] demonstrate the generation of magnetostatic waves in thin metallic films by the δM-process. The authors of [201, 202] used the $\delta\varepsilon$-process to generate magnetoelastic waves in Co:YIG. We think that generating magnetostatic waves by laser-induced variation of anisotropy provides much broader opportunities and should be the subject of future research.

Optically-induced spin pumping. Precessing magnetization can inject spin current into a layer of a nonmagnetic material bordering the magnetic layer [203]. Spin pumping plays an important role in spin valve-like structures (Fig. 19a), where it maintains dynamic links between ferromagnetic layers, which are independent in the static case. A spin current injected through a nonmagnetic interlayer from one ferromagnetic layer to another can induce stimulated magnetization precession in the latter. Of special interest is a regime with similar precession eigenfrequencies in the two ferromagnetic layers and spin pumping responsible for the *dissipative* character of dynamic coupling between them.

In the case of two dissipatively coupled oscillators under resonance conditions in which their frequencies coincide, the two coupled frequency-degenerate modes have different lifetimes. When two precessing magnetizations are coupled by the spin pumping effect, one of the modes with a long lifetime can be regarded as the precession of two magnetizations in phase with each other and the other short-lived one as the out-of-phase precession of two magnetizations (Fig. 19b). The damping coefficient of the first mode corresponds to intrinsic damping of precession α of an isolated magnetic film. The damping coefficient of the second rapidly decaying mode is $\alpha + 2\beta$, where β is damping due to the generation of spin current.

Dissipative coupling is based on the fact that reciprocal spin pumping under conditions of coincident frequencies of precessions strengthens/weakens precession damping $\alpha \pm \beta$, depending on their relative initial phases. Here, $\pm\beta$ is the addition to Gilbert damping α resulting from spin pumping. Such a coupling manifests itself in the formation of two coupled frequency-degenerate modes with different damping characteristics (Fig. 19b).

Reference [204] reports the first experimental demonstration of excitation and detection of both coupled precession modes in the epitaxial structure of an FeGa/Cu(5 nm)/FeGa pseudo-spin valve on a GaAs(100) substrate (Fig. 19a). In such a structure, FeGa layers have different anisotropies, and the dependences of precession frequency on the external field direction in the structure plane differ. Variation in the direction of the external field $\mathbf{H}_{ext}$ leads to precession frequency detuning in the two layers or resonance between them. Precessions excited in these two layers by the δK-process are characterized in the general case by different amplitudes and initial phases ϕ_0, with the relationship between them being dependent on the direction of the external magnetic field. By orienting this field in the film plane, the authors of [204] were able to independently excite magnetization precession in the two layers of FeGa/Cu(5 nm)/FeGa by the δK-process with a small contribution β of mutual spin pumping to precession damping. However, when the $\mathbf{H}_{ext}$ orientation meets the near-resonance condition between the two precessions, the magnetization dynamics (Fig. 19c) was a superposition of two precessing contributions (Figs 19d, e) with long and short lifetimes, respectively, that were actually two modes dissipatively couple due to spin pumping (Fig. 19b). It should be emphasized that magnetizations linked by spin pumping present a rare example of the experimental system in which the purely dissipative coupling between two oscillators is realized.

6.3.3 Resonant phonon pumping of precession and generation of a localized microwave field. One of the striking manifestations of the $\delta\varepsilon$-process of magnetic anisotropy modulation is resonant pumping of magnetization precession by localized monochromatic phonons and the generation of an alternating magnetic field based on this mechanism. Phonon (elastic) self-resonances of a ferromagnetic structure with a characteristic

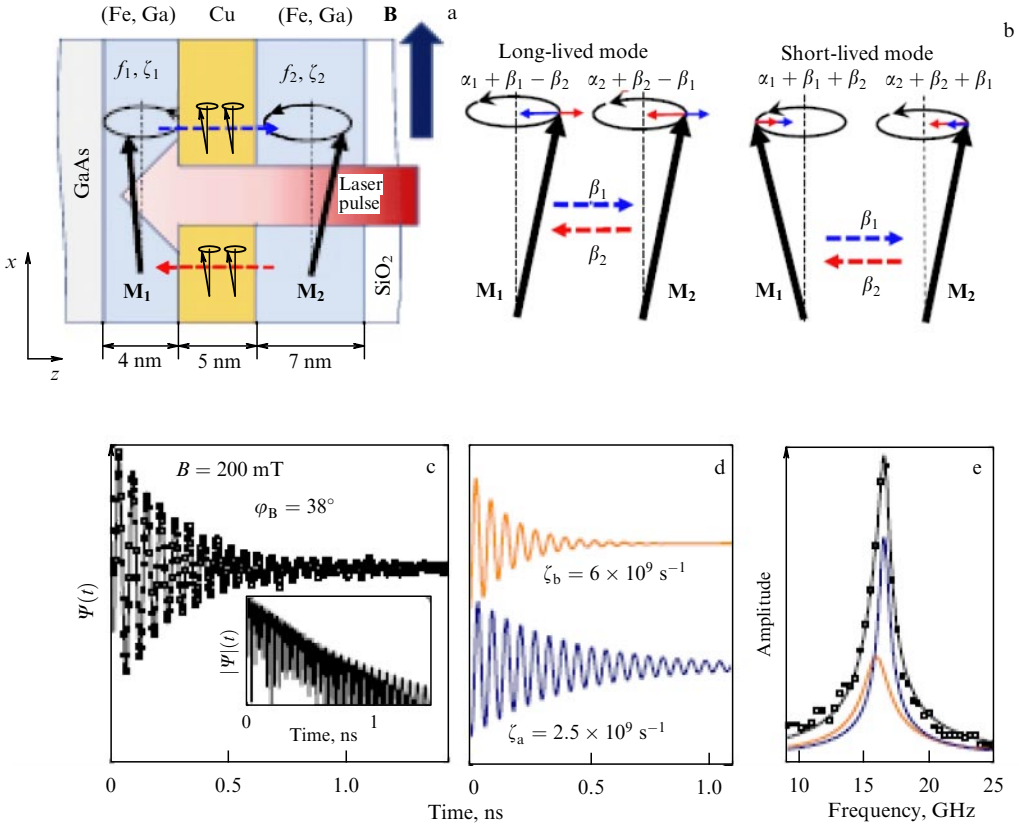

Figure 19. (Color online.) Optically induced spin pumping and formation of dissipatively coupled modes in an FeGa/Cu/FeGa/GaAs(001) spin valve [204]. (a) Schematics of the studied structure. (b) Schematic representation of magnetization of individual layers in long- and short-living dissipatively coupled modes. (c) Time dependence of the polar MO Kerr effect measured near the resonance between precession frequencies in two (Fe,Ga) layers. (d, e) Decomposition of the signal presented in Fig. c into two components with identical frequencies but different decays.

size of 10–100 nm lie in the frequency range between 10 and 100 GHz. Phonons of these frequencies are excited by a femtosecond laser pulse within a broad coherent wave packet generated by ultrafast heating of the crystal lattice. Elastic oscillations at nonresonant frequencies rapidly decay or leave the ferromagnet structure, whereas eigenmodes may have lifetimes as long as a few tens and even hundreds of nanoseconds. Given that the magnetoacoustic resonance condition is fulfilled at which the localized phonon frequency coincides with the precession frequency, the phonon pumping effect takes place, maintaining precession throughout the entire lifetime of localized phonons. This effect can be used to generate high-frequency alternating spin currents and magnetic fields with a narrow spectral band.

Spatially periodic structures are used to achieve a high Q-factor of phonon resonance at sub-terahertz frequencies. In the first work on resonant phonon pumping of precession [205], a 60-nm-thick ferromagnetic layer of galfenol was grown on a GaAs/AlAs semiconductor superlattice that served as a Bragg mirror for phonons with a frequency of roughly 20 GHz, corresponding to the minimal-frequency resonance of the ferromagnetic film of the chosen thickness. The open surface on the opposite side played the role of a second phonon mirror by forming a Fabri–Perot phonon resonator with a Q-factor of ~ 100. Excitation of the structure by a femtosecond laser pulse caused the generation of localized monochromatic elastic oscillations in the ferromagnetic layer that, in turn, induced magnetization precession by modulating the magnetocrystalline anisotropy. The maximum forced precession amplitude was reached under the resonance conditions when the external magnetic field-controlled oscillation frequency of free precession coincided with the localized phonon mode frequency. The magnetization oscillation lifetime was determined by the phonon resonance quality factor.

Long-lived elastic oscillations of sub-terahertz frequencies can be excited in structures with lateral spatial periodicity. In Ref. [206], magnetization precession was maintained by surface monochromatic elastic oscillations excited in a one-dimensional ferromagnetic nanograting formed by parallel grooves having width and depth of 40 nm with a repetition of 150 nm produced by the ion etching technique on an area 5×5 μm^2 in a galfenol film 10 nm in thickness. The frequency of the surface phonon mode localized in this structure was 15 GHz and the lifetime longer than 5 ns. Figures 20a, b show the temporal evolution of magnetization and the respective Fourier spectra obtained under the conditions of excitation of the ferromagnetic film by a laser pulse outside (the upper curve) and inside the nanograting at three values of the external magnetic field (three lower curves). Under the resonance conditions ($B = 175$ mT), the spectral amplitude of precession reached its maximum. An important characteristic of such a structure was the generation of a microwave magnetic field by precessing magnetization outside the ferromagnetic layer. The spatial distribution of two components of the alternating field being generated is shown in Figs 20c, d. The induced 15-mT alternating magnetic field was localized in a 40×40-nm^2 groove. This combination of large

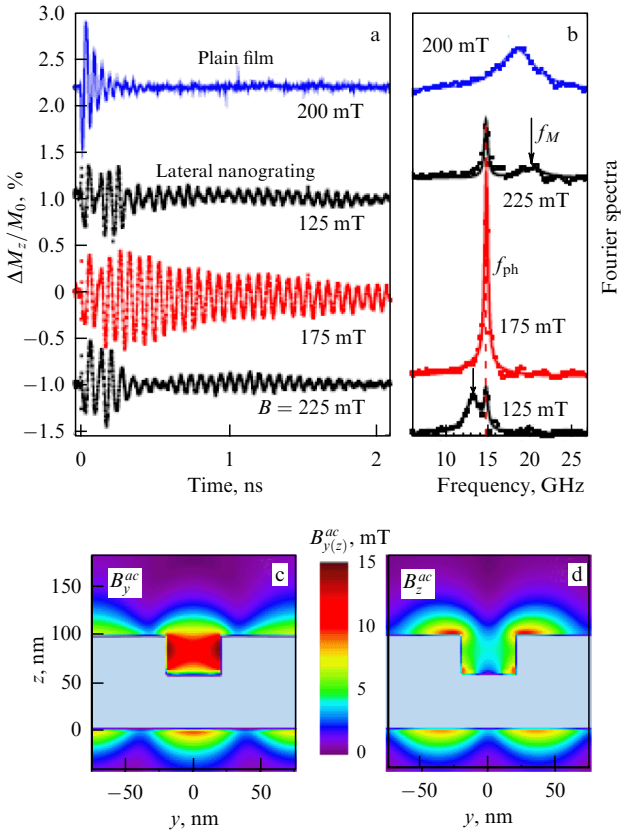

Figure 20. (Color online.) (a) Laser-induced magnetization precession. (b) Corresponding Fourier spectra in plain galfenol film (upper curve) and a lateral nanograting at three values of the external magnetic field (three lower curves). (c, d) Calculated distribution of two projections of an alternating magnetic field generated by precessing magnetization in a nanograting within one spatial period [206].

amplitude and nanometer localization can be used to control single spins (e.g., NV centers in diamonds) or in magnetic resonance tomography with nanometer resolution.

7. Conclusions

The present review considers several striking and urgent problems facing the spintronics of metallic, semiconductor, and dielectric heterostructures. An important issue in semiconductor spintronics to date is the spin polarization control and creating magnetically ordered semiconducting structures with properties allowing them to be integrated into semiconductor electronics. The major advantage of such structures is the possibility of controlling their magnetic order by an electric field or current with the prospect of designing a 'single-chip computer'. We considered two approaches to the solution of this problem based on the development and control of the properties of diluted magnetic semiconductors or the fabrication of hybrid systems consisting of thin ferromagnetic metallic films and semiconductors exhibiting the proximity effect. Several mechanisms underlying the formation of the proximity effect in hybrid structures were discussed, including the recently discovered long-range proximity effect based on the possibility of exciting elliptically polarized phonons in semiconductor/ferromagnet structures.

A special branch in the development of semiconductor spintronics opening the way to the development of new quantum technologies is coherent control of single spins, first of all in color centers of diamonds and silicon carbide. We considered advancements in this field achieved by the application of ultrasensitive optical methods for obtaining and detecting high-resolution images and reliable coherent control with the use of nuclear magnetic resonance. Approaches to the scaling of color centers with high accuracy and precision and the realization of long coherence times were discussed with reference to new possibilities that they open up for so-called hybrid quantum processes in which color centers are coupled with different types of qubits.

Switching of magnetization in separate ferromagnetic elements by electric field pulses is a fundamental element in the spintronics of metallic materials. It can be employed to create all-metal electronic devices with prospects for their miniaturization and improvement of heat removal. Several switching mechanisms for the purpose are considered. The switching of a ferromagnet is possible by injecting spin-polarized current. Moreover, the indirect exchange interaction of two ferromagnetic elements can be governed taking advantage of the impact of the nonequilibrium electron distribution function; in the absence of a Coulomb blockade, it is possible without passing electric current through the system. A novel approach to controlling metallic heterostructures with ferrimagnetically ordered elements is switching by picosecond pulses of electric current, which causes pulsed heating of the system. In this case, switching is achieved by delicate control of the balance between exchange inter-electron scattering times, spin relaxation time, and electron subsystem heating time.

A separate section of this review is devoted to an innovative branch of spintronics, ultrafast magnetism. We discussed progress in control of magnetization in magnetic structures by femtosecond laser pulses, with special reference to the laser-induced change of magnetic anisotropy observed in materials with various electronic and magnetic structures. We believe that this area opens up wide prospects for application in different structures promising for the purposes of spintronics. Specifically, the possibilities of optical excitation of magnetic precession modes, generating high-frequency localized magnetic fields, and switching of magnetization were discussed.

Acknowledgements. V F S thanks N S Averkiev, I V Krainov, G S Dmitriev, and K H Ploog for fruitful cooperation in DMS research; A M K, R V P, and A V Sch thank A V Kimel, A Kirilyuk, T Rasing, A M Balbashov, J A de Jong, I Razdorski, D Afanasiev, B A Ivanov, A Stupakewicz, A Maziewsky, F Atoneche, A V Akimov, A W Rushforth, T L Linnik, B A Glavin, S Koukhtaruk, L A Shelukhin, A S Salasyuk, V N Kats, N E Khokhlov, V V Pavlov, and P A Usachev for cooperation in research on laser-induced ultrafast processes in magnetic media. The authors acknowledge financial support from the Russian Science Foundation (grants nos 18-12-00352 (Yu G K and V F S) for investigations of the effect of strain on magnetization of ferromagnetic semiconductors, 16-12-10485 (A V Sch), and 16-12-10456 (R V P); the Russian Foundation for Basic Research (grant Nos 15-52-12017-NNIO-a (V F S), 19-52-12034-NNIO-a (V L K), 15-52-12015-NNIO-a (A M K), 16-02-00064-a (V I K), and 18-02-0082-a (A M K); the Government of the Russian Federation (grant no. 14.Z50.31.0021 (M B, P G B) and Deutsche Forschungsgemeinschaft (TRR-160 ICRC project) (I A A, D R Ya, M B).

References

1. \check {\rm Z}\uti\acute {\rm c}*Ietal.Rev.Mod.Phys.***76**323(2004)
2. Kusrayev Yu G *Phys. Usp.* **53** 725 (2010); *Usp. Fiz. Nauk* **180** 759 (2010)
3. Ivchenko E L *Phys. Usp.* **55** 809 (2012); *Usp. Fiz. Nauk* **182** 869 (2012)
4. Baibich M N et al. *Phys. Rev. Lett.* **61** 2472 (1988)
5. Binasch G et al. *Phys. Rev. B* **39** 4828(R) (1989)
6. Parkin S et al. *Proc. IEEE* **91** 661 (2003)
7. Apalkov D et al. *Proc. IEEE* **104** 1796 (2016)
8. Parkin S, Yang S-H *Nature Nanotechnol.* **10** 195 (2015)
9. Silva T, Rippard W *J. Magn. Magn. Mater.* **320** 1260 (2008)
10. Chumak A V et al. *Nature Phys.* **11** 453 (2015)
11. Nikitov S A et al. *Phys. Usp.* **58** 1002 (2015); *Usp. Fiz. Nauk* **185** 1099 (2015)
12. Jungwirth T et al. *Nature Phys.* **14** 200 (2018)
13. Jungfleisch M B, Zhang W, Hoffmanna A *Phys. Lett. A* **382** 865 (2018)
14. Pyatakov A P, Zvezdin A K *Phys. Usp.* **55** 557 (2012); *Usp. Fiz. Nauk* **182** 593 (2012)
15. Pyatakov A P et al. *Phys. Usp.* **58** 981 (2015); *Usp. Fiz. Nauk* **185** 1077 (2015)
16. Bauer G E W, Saitoh E, van Wees B J *Nature Mater.* **11** 391 (2012)
17. Kirilyuk A, Kimel A V, Rasing T *Rev. Mod. Phys.* **82** 2731 (2010)
18. Averyanov D V et al. *ACS Appl. Mater. Interfaces* **7** 6146 (2015)
19. Furdyna J K *J. Appl. Phys.* **64** R29 (1988)
20. Story T et al. *Phys. Rev. Lett.* **56** 777 (1986)
21. Karlik I Ya et al. *Sov. Phys. Solid State* **24** 2022 (1982); *Fiz. Tverd. Tela* **24** 3550 (1982)
22. Masterov V F et al. *Sov. Phys. Semicond.* **17** 796 (1983); *Fiz. Tekh. Poluprovodn.* **17** 1259 (1983)
23. Schneider J et al. *Phys. Rev. Lett.* **59** 240 (1987)
24. Averkiev N S et al. *Sov. Phys. Solid State* **30** 438 (1988); *Fiz. Tverd. Tela* **30** 765 (1988)
25. Sapega V F, Ruf T, Cardona M *Solid State Commun.* **114** 573 (2000)
26. Sapega V F, Ruf T, Cardona M *Phys. Status Solidi B* **226** 339 (2001)
27. Munekata H et al. *Phys. Rev. Lett.* **63** 1849 (1989)
28. Ohno H et al. *Phys. Rev. Lett.* **68** 2664 (1992)
29. Ohno H et al. *Appl. Phys. Lett.* **69** 363 (1996)
30. Hayashi T et al. *J. Cryst. Growth* **175–176** 1063 (1997)
31. Van Esch A et al. *Phys. Rev. B* **56** 13103 (1997)
32. Chen L et al. *Nano Lett.* **11** 2584 (2011)
33. Ohno Y et al. *Nature* **402** 790 (1999)
34. Chiba D et al. *Science* **301** 943 (2003)
35. Ciorga M et al. *New J. Phys.* **9** 351 (2007)
36. Ciorga M et al. *Phys. Rev. B* **79** 165321 (2009)
37. Stolichnov I et al. *Nature Mater.* **7** 464 (2008)
38. Korenev V L et al. *Nature Commun.* **3** 959 (2012)
39. Vila L et al. *Phys. Rev. Lett.* **98** 027204 (2007)
40. Endres B et al. *Nature Commun.* **4** 2068 (2013)
41. Gorchon J et al. *Phys. Rev. Lett.* **112** 026601 (2014)
42. Dietl T, Ohno H, Matsukura F *Phys. Rev. B* **63** 195205 (2001)
43. Dietl T et al. *Science* **287** 1019 (2000)
44. Jungwirth T et al. *Phys. Rev. B* **72** 165204 (2005)
45. Neumaier D et al. *Phys. Rev. Lett.* **103** 087203 (2009)
46. Hirakawa K et al. *Phys. Rev. B* **65** 193312 (2002)
47. Burch K S et al. *Phys. Rev. Lett.* **97** 087208 (2006)
48. Sapega V F et al. *Phys. Rev. Lett.* **94** 137401 (2005)
49. Ando K et al. *Phys. Rev. Lett.* **100** 067204 (2008)
50. Rokhinson L P et al. *Phys. Rev. B* **76** 161201(R) (2007)
51. Alberi K et al. *Phys. Rev. B* **78** 075201 (2008)
52. Ohya S, Takata K, Tanaka M *Nature Phys.* **7** 342 (2011)
53. Akai H *Phys. Rev. Lett.* **81** 3002 (1998)
54. Haiml M et al. *Appl. Phys. Lett.* **74** 1269 (1999)
55. Němec H et al. *J. Appl. Phys.* **90** 1303 (2001)
56. Sapega V F et al. *Phys. Rev. B* **73** 235208 (2006)
57. Liu X, Furdina J K *J. Phys. Condens. Matter* **18** R245 (2006)
58. Alekseev M A et al. *Sov. Phys. Semicond.* **23** 479 (1989); *Fiz. Tekh. Poluprovodn.* **23** 761 (1989)
59. Sapega V F et al. *Phys. Rev. B* **80** 041202(R) (2009)
60. Shen A et al. *J. Cryst. Growth.* **175–176** 1069 (1997)
61. Welp U et al. *Phys. Rev. Lett.* **90** 167206 (2003)
62. Sapega V F et al. *Solid State Commun.* **157** 34 (2013)
63. Krainov I V et al. *Phys. Rev. B* **93** 235202 (2016)
64. Kimel A V et al. *Phys. Rev. Lett.* **92** 237203 (2004)
65. Mitsumori Y et al. *Phys. Rev. B* **69** 033203 (2004)
66. Wang D M et al. *Phys. Rev. B* **75** 233308 (2007)
67. Rubinstein M et al. *J. Magn. Magn. Mater.* **250** 164 (2002)
68. Sinova J et al. *Phys. Rev. B* **69** 085209 (2004)
69. Bombeck M et al. *Phys. Rev. B* **85** 195324 (2012)
70. Krainov I V et al. *Phys. Rev. B* **92** 245201 (2015)
71. Jungwirth T et al. *Rev. Mod. Phys.* **78** 809 (2006)
72. Kittel C *Phys. Rev.* **115** 1587 (1959)
73. Zakharchenya B P, Korenev V L *Phys. Usp.* **48** 603 (2005); *Usp. Fiz. Nauk* **175** 629 (2005)
74. Korenev V L *JETP Lett.* **78** 564 (2003); *Pis'ma Zh. Eksp. Teor. Fiz.* **78** 1053 (2003)
75. Dzhioev R I et al. *JETP Lett.* **60** 661 (1994); *Pis'ma Zh. Eksp. Teor. Fiz.* **60** 650 (1994)
76. Dzhioev R I, Zakharchenya B P, Korenev V L *Phys. Solid State* **37** 1929 (1995); *Fiz. Tverd. Tela* **37** 3510 (1995)
77. Korenev V L *Solid State Commun.* **102** 13 (1997)
78. Korenev V L *Semicond. Sci. Technol.* **23** 114012 (2008)
79. Myers R C, Gossard A C, Awschalom D D *Phys. Rev. B* **69** 161305(R) (2004)
80. Zaitsev S V et al. *JETP Lett.* **90** 658 (2010); *Pis'ma Zh. Eksp. Teor. Fiz.* **90** 730 (2009)
81. Korenev V L et al. *Nature Phys.* **12** 85 (2016)
82. Pankov M A et al. *JETP* **109** 293 (2009); *Zh. Eksp. Teor. Fiz.* **136** 346 (2009)
83. Korenev V L et al. *Nature Commun.* **3** 959 (2012)
84. Akimov I A et al. *Phys. Rev. B* **96** 184412 (2017)
85. Ladd T D et al. *Nature* **464** 45 (2010)
86. Elzerman J M et al. *Nature* **430** 431 (2004)
87. Xiao M et al. *Nature* **430** 435 (2004)
88. Rugar D et al. *Nature* **430** 329 (2004)
89. Köhler J et al. *Nature* **363** 242 (1993)
90. Wrachtrup J et al. *Nature* **363** 244 (1993)
91. Gruber A et al. *Science* **276** 2012 (1997)
92. Baranov P G et al. *JETP Lett.* **82** 441 (2005); *Pis'ma Zh. Eksp. Teor. Fiz.* **82** 494 (2005)
93. Baranov P G et al. *JETP Lett.* **86** 202 (2007); *Pis'ma Zh. Eksp. Teor. Fiz.* **86** 231 (2007)
94. Weber J R et al. *Proc. Natl. Acad. Sci. USA* **107** 8513 (2010)
95. Baranov P G et al. *Phys. Rev. B* **83** 125203 (2011)
96. Riedel D et al. *Phys. Rev. Lett.* **109** 226402 (2012)
97. Kraus H et al. *Sci. Rep.* **4** 5303 (2014)
98. Kraus H et al. *Nature Phys.* **10** 157 (2014)
99. Simin D et al. *Phys. Rev. X* **6** 031014 (2016)
100. Widmann M et al. *Nature Mater.* **14** 164 (2015)
101. Christle D J et al. *Nature Mater.* **14** 160 (2015)
102. Baranov P G et al. *Magnetic Resonance of Semiconductors and Their Nanostructures*: *Basic and Advanced Applications* (Springer Series in Materials Science, Vol. 253) (Vienna: Springer, 2017)
103. Orrit M *J. Chem. Phys.* **117** 10938 (2002)
104. Santori C et al. *Phys. Rev. Lett.* **97** 247401 (2006)
105. Buckley B B et al. *Science* **330** 1212 (2010)
106. Togan E et al. *Nature* **466** 730 (2010)
107. Anisimov A N et al. *Sci. Rep.* **6** 33301 (2016)
108. Soltamov V A et al. *Phys. Rev. Lett.* **115** 247602 (2015)
109. Anisimov A N et al. *Appl. Magn. Reson.* **49** 85 (2018)
110. Soltamov V A, Baranov P G *Phys. Usp.* **59** 605 (2016); *Usp. Fiz. Nauk* **186** 678 (2016)
111. Mistry K et al., in *2007 IEEE Intern. Electron Devices Meeting, Washington, DC, 2007*, p. 247, https://doi.org/10.1109/IEDM.2007.4418914
112. Slonczewski J C *J. Magn. Magn. Mater.* **159** L1 (1996)
113. Myers E B et al. *Science* **285** 867 (1999)
114. Theeuwen S J C H et al. *Appl. Phys. Lett.* **75** 3677 (1999)
115. Katine J A et al. *Phys. Rev. Lett.* **84** 3149 (2000)
116. Waintal X et al. *Phys. Rev. B* **62** 12317 (2000)
117. Zhang S, Levy P M, Fert A *Phys. Rev. Lett.* **88** 236601 (2002)
118. Stiles M D, Zangwill A *Phys. Rev. B* **66** 014407 (2002)
119. Slonczewski J C *J. Magn. Magn. Mater.* **247** 324 (2002)
120. Barnaś J et al. *Phys. Rev. B* **72** 024426 (2005)

121. Tserkovnyak Y, Brataas A, Bauer E W *Phys. Rev. Lett.* **88** 117601 (2002)
122. Tserkovnyak Y, Brataas A, Bauer E W *Phys. Rev. B* **66** 224403 (2002)
123. Tserkovnyak Y, Brataas A, Bauer E W *Phys. Rev. B* **67** 140404(R) (2003)
124. Gulyaev Yu V, Zil berman P E, Epshtein E M *Phys. Usp.* **51** 409 (2008); *Usp. Fiz. Nauk* **178** 433 (2008)
125. Zvezdin A K, Zvezdin K A, Khval kovskii A V *Phys. Usp.* **51** 412 (2008); *Usp. Fiz. Nauk* **178** 436 (2008)
126. Berger L *Phys. Rev. B* **54** 9353 (1996)
127. Kozub V I, Caro J *Phys. Rev. B* **76** 224425 (2007)
128. Gantsevich S V et al. *Phys. Status Solidi B* **75** 407 (1976)
129. Schwabe N F, Elliott R J, Wingreen N S *Phys. Rev. B* **54** 12953 (1996)
130. You C-Y, Bader S D *J. Magn. Magn. Mater.* **195** 488 (1999)
131. Heide C, Elliott R J, Wingreen N S *Phys. Rev. B* **59** 4287 (1999)
132. Heide C, Eliott R J *Europhys. Lett.* **50** 271 (2000)
133. Kozub V I, Vinokur V *Appl. Phys. Lett.* **87** 062507 (2005)
134. Kittel Ch *Quantum Theory of Solids* (New York: Wiley, 1963)
135. Kulik I O, Shekhter R I, Omelyanchouk A N *Solid State Commun.* **23** 301 (1977)
136. Baltensperger W, Helman J S *Appl. Phys. Lett.* **57** 2954 (1990)
137. Kozub V I, Galperin Y M, Vinokur V M *J. Magn. Magn. Mater.* **465** 304 (2018)
138. Stanciu C D et al. *Phys. Rev. Lett.* **99** 047601 (2007)
139. Vahaplar K et al. *Phys. Rev. Lett.* **103** 117201 (2009)
140. Ostler T A et al. *Nature Commun.* **3** 666 (2012)
141. Khorsand A R et al. *Phys. Rev. Lett.* **108** 127205 (2012)
142. Radu I et al. *Nature* **472** 205 (2011)
143. Kalashnikova A M, Kozub V I *Phys. Rev. B* **93** 054424 (2016)
144. Yang Y et al. *Sci. Adv.* **3** e1603117 (2017)
145. Beaurepaire E et al. *Phys. Rev. Lett.* **76** 4250 (1996)
146. Kalashnikova A M, Kimel A V, Pisarev R V *Phys. Usp.* **58** 969 (2015); *Usp. Fiz. Nauk* **185** 1064 (2015)
147. Bossini D et al. *ACS Photon.* **3** 1385 (2016)
148. Carva K, Baláž P, Radu I, in *Handbook of Magnetic Materials* Vol. 26 (Ed. E Brück) (Amsterdam: Elsevier, 2017) p. 291
149. Linnik T L et al. *Phys. Scripta* **92** 054006 (2017)
150. Němec P et al. *Nature Phys.* **14** 229 (2018)
151. Gerrits Th et al. *Nature* **418** 509 (2002)
152. Vogel M et al. *Nature Phys.* **11** 487 (2015)
153. Acremann Y et al. *Science* **290** 492 (2000)
154. Carpene E et al. *Phys. Rev. B* **81** 060415(R) (2010)
155. Carpene E et al. *J. Appl. Phys.* **108** 063919 (2010)
156. Tesařová N et al. *Appl. Phys. Lett.* **100** 102403 (2012)
157. van Kampen M et al. *Phys. Rev. Lett.* **88** 227201 (2002)
158. Koopmans B et al. *Phys. Rev. Lett.* **85** 844 (2000)
159. Koopmans B et al. *Nature Mater.* **9** 259 (2010)
160. Mendil J et al. *Sci. Rep.* **4** 3980 (2014)
161. Kaganov M I et al. *Sov. Phys. JETP* **4** 173 (1957); *Zh. Eksp. Teor. Fiz.* **31** 232 (1957)
162. Zener C *Phys. Rev.* **96** 1335 (1954)
163. Becker J et al. *Appl. Phys. Lett.* **104** 152412 (2014)
164. Kimel A V et al. *Phys. Rev. Lett.* **89** 287401 (2002)
165. Shelukhin L A et al. *Phys. Rev. B* **97** 014422 (2018)
166. Kimel A V et al. *Nature* **435** 655 (2005)
167. Hashimoto Y, Kobayashi S, Munekata H *Phys. Rev. Lett.* **100** 067202 (2008)
168. Matsuda T, Munekata H *Phys. Rev. B* **93** 075202 (2016)
169. Qi J et al. *Phys. Rev. B* **79** 085304 (2009)
170. Belov K P et al. *Sov. Phys. Usp.* **19** 574 (1976); *Usp. Fiz. Nauk* **119** 447 (1976)
171. Kimel A V et al. *Nature* **429** 850 (2004)
172. Kimel A V et al. *Phys. Rev. B* **74** 060403(R) (2006)
173. de Jong J A et al. *Phys. Rev. B* **84** 104421 (2011)
174. de Jong J A et al. *J. Phys. Condens. Matter* **29** 164004 (2017)
175. Scherbakov A V et al. *Phys. Rev. Lett.* **105** 117204 (2010)
176. Thomsen C et al. *Phys. Rev. B* **34** 4129 (1986)
177. Kim J-W, Vomir M, Bigot J-Y *Phys. Rev. Lett.* **109** 166601 (2012)
178. Deb M et al. *Phys. Rev. B* **98** 174407 (2018)
179. Afanasiev D et al. *Phys. Rev. Lett.* **112** 147403 (2014)
180. Janušonis J et al. *Sci. Rep.* **6** 29143 (2016)
181. Kats V N et al. *Phys. Rev. B* **93** 214422 (2016)
182. Reid A H et al. *Nature Commun.* **9** 388 (2018)
183. Young E S K et al. *Phys. Rev. B* **86** 155207 (2012)
184. Kovalenko V F, Nagaev E L *Sov. Phys. Usp.* **29** 297 (1986); *Usp. Fiz. Nauk* **148** 561 (1986)
185. Stupakiewicz A et al. *Phys. Rev. B* **64** 064405 (2001)
186. Hansteen F et al. *Phys. Rev. Lett.* **95** 047402 (2005)
187. Le J-L, Bažant Z P, Bazant M Z *J. Phys. D* **42** 105003 (2009)
188. Atoneche F et al. *Phys. Rev. B* **81** 214440 (2010)
189. Stupakiewicz A et al. *Nature Commun.* **10** 612 (2019)
190. Stupakiewicz A et al. *Nature* **542** 71 (2017)
191. Kimel A V et al. *Nature Phys.* **5** 727 (2009)
192. de Jong J A et al. *Phys. Rev. Lett.* **108** 157601 (2012)
193. Le Guyader L et al. *Phys. Rev. B* **87** 054437 (2013)
194. Afanasiev D et al. *Phys. Rev. Lett.* **116** 097401 (2016)
195. Kalashnikova A M et al. *Phys. Rev. Lett.* **99** 167205 (2007)
196. Afanasiev D, Zvezdin A K, Kimel A V *Opt. Express* **23** 23978 (2015)
197. Satoh T et al. *Nature Photon.* **6** 662 (2012)
198. Au Y et al. *Phys. Rev. Lett.* **110** 097201 (2013)
199. Kamimaki A et al. *Phys. Rev. B* **96** 014438 (2017)
200. Yun S-J, Cho C-G, Choe S-B *Appl. Phys. Exp.* **8** 063009 (2015)
201. Hashimoto Y et al. *Nature Commun.* **8** 15859 (2017)
202. Hashimoto Y et al. *Phys. Rev. B* **97** 140404(R) (2018)
203. Tserkovnyak Y et al. *Rev. Mod. Phys.* **77** 1375 (2005)
204. Danilov A P et al. *Phys. Rev. B* **98** 060406(R) (2018)
205. Jäger J V et al. *Phys. Rev. B* **92** 020404(R) (2015)
206. Salasyuk A S et al. *Phys. Rev. B* **97** 060404(R) (2018)